UCLA/13/TEP/111 SLAC–PUB–15870 SB/F/434–13 IPhT–T13/270
IPPP/13/1 FR-PHENO-2014-001

Next-to-Leading Order $\gamma\gamma$ + 2-Jet Production at the LHC

Z. Bern[a], L. J. Dixon[b], F. Febres Cordero[c], S. Höche[b],
H. Ita[d], D. A. Kosower[e], N. A. Lo Presti[e] and D. Maître[f]

[a]Department of Physics and Astronomy, UCLA, Los Angeles, CA 90095-1547, USA
[b]SLAC National Accelerator Laboratory, Stanford University, Stanford, CA 94309, USA
[c]Departamento de Física, Universidad Simón Bolívar, Caracas 1080A, Venezuela
[d]Physikalisches Institut, Albert-Ludwigs-Universität Freiburg, D–79104 Freiburg, Germany
[e]Institut de Physique Théorique, CEA–Saclay, F–91191 Gif-sur-Yvette cedex, France
[f]Department of Physics, University of Durham, Durham DH1 3LE, UK

arXiv:1402.4127v1 [hep-ph] 17 Feb 2014

Abstract

We present next-to-leading order QCD predictions for cross sections and for a comprehensive set of distributions in $\gamma\gamma$ + 2-jet production at the Large Hadron Collider. We consider the contributions from loop amplitudes for two photons and four gluons, but we neglect top quarks. We use BlackHat together with SHERPA to carry out the computation. We use a Frixione cone isolation for the photons. We study standard sets of cuts on the jets and the photons, and also sets of cuts appropriate for studying backgrounds to Higgs-boson production via vector-boson fusion.

PACS numbers: 12.38.-t, 12.38.Bx, 13.87.-a, 14.70.Bh

I. INTRODUCTION

Reliable theoretical predictions for Standard-Model processes at the Large Hadron Collider (LHC) are important to ongoing searches for new physics. They are also important to the increasingly precise studies of the recently discovered Higgs-like boson [1], of the top quark, and of vector boson self-interactions. Uncovering hints of new physics beyond the Standard Model requires a good quantitative understanding of the Standard-Model backgrounds and their uncertainties.

Predictions for background rates at the LHC rely on perturbative QCD, which enters all aspects of short-distance collisions at a hadron collider. Leading-order (LO) predictions in QCD suffer from a strong dependence on the unphysical renormalization and factorization scales. This dependence gets stronger with increasing jet multiplicity. Next-to-leading order (NLO) results generally reduce this dependence dramatically, typically to a 10–15% residual sensitivity. Thus they offer the first quantitatively reliable order in perturbation theory.

Photon pairs are a key decay channel for detecting and measuring the Higgs-like boson. A good understanding of prompt photon-pair background is important for precision measurements of its properties and for uncovering deviations from Standard Model expectations. In particular, when the photon pair is produced in association with two hadronic jets, the process is an important background to Higgs-like boson production via vector-boson fusion (VBF). We study this background in the present paper, both for standard cuts on the jets and the photons, as well as for other sets of cuts designed to isolate the VBF region of phase space.

Inclusive photon-pair production was studied at NLO by a number of groups [2, 3]. Gluon-initiated subprocesses, which arise only at one loop, account for an important fraction of the cross section. Studying these subprocesses to their NLO requires two-loop amplitudes [4], which have been applied to photon-pair production [5]. More recently, NNLO results for inclusive di-photon production have been presented by Catani, Cieri, de Florian, Ferrera and Grazzini [6]. NLO predictions for the production of a photon pair in association with a single jet were given some time ago [7, 8]. Here we present predictions for inclusive photon-pair production in association with two jets at NLO. This process has also been studied recently by Gehrmann, Greiner, and Heinrich (GGH) [9], and by Badger, Guffanti and Yundin [10]. (The latter paper also provides NLO results for photon-pair production in association with

three jets.) We study three pairs of cuts. Each pair consists of a standard jet cut, and a cut appropriate for isolating Higgs bosons formed from vector boson fusion. The second and third pairs of cuts are oriented toward specific experimental analyses by the ATLAS and CMS collaborations.

In the present paper we use on-shell methods as implemented in numerical form in the BlackHat software library [11]. This library, together with the SHERPA package [12], has previously been used to make NLO predictions for a variety of vector boson plus multi-jet production processes [13–17], most recently for W + 5-jets [18], and for four-jet production [19]. It has also been used to compute γ + n-jet to Z + n-jet ratios for assessing theoretical uncertainties [20, 21] in the CMS searches [22] for supersymmetric particles. The ATLAS collaboration has also used results from BlackHat computations with SHERPA for Standard-Model studies of electroweak vector-boson production in association with three or more jets [23]. Other programs that use on-shell methods are described in refs. [24, 25].

SHERPA is used to manage the numerous partonic subprocesses entering the calculation, to integrate over phase space, to construct physical distributions, and to output ROOT [26] n-tuples. We use the COMIX package [27] to compute Born and real-emission matrix elements, along with the corresponding Catani–Seymour [28] dipole subtraction terms. Rather than repeating the entire computation for each scale and for each parton distribution function (PDF) set, we store intermediate results in n-tuple format, recording momenta for all partons in an event, along with the coefficients of various scale- or PDF-dependent functions in the event weight [29]. The n-tuple storage makes it possible to evaluate cross sections and distributions for different scales and PDF error sets. We have generated two sets of n-tuples, one corresponding to loose standard jet cuts, and another adding VBF cuts. We are then able to study modifications of each of these cuts without the time-consuming recomputation of matrix elements. The n-tuples generated for the present study are available in the format of ref. [29] with process directories `YY2j` and `YY2j_VBF`.

This paper is organized as follows. In section II we summarize the basic setup of the computation. In section III we present our results for cross sections, ratios and distributions. We summarize and give our conclusions in section IV. Tables for distributions are in three appendices. A fourth appendix contains matrix elements at a point in phase space.

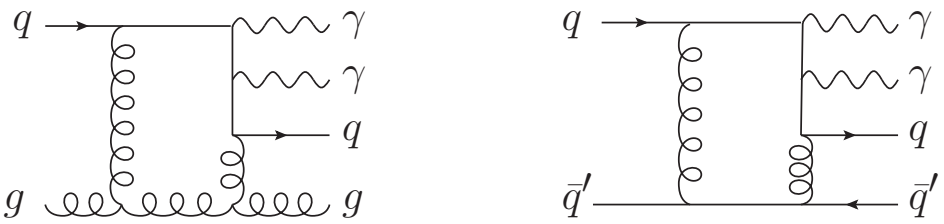

FIG. 1: Examples of six-point loop diagrams for the processes $qg \to \gamma\gamma qg$ and $q\bar{q}' \to \gamma\gamma q\bar{q}'$.

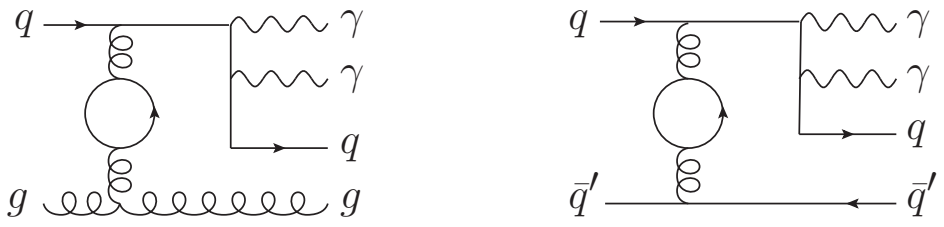

FIG. 2: Examples of six-point fermion-loop diagrams for the processes $qg \to \gamma\gamma qg$ and $q\bar{q}' \to \gamma\gamma q\bar{q}'$. These diagrams have a closed quark loop, but the photons do not couple directly to it.

II. BASIC SETUP

In this paper we compute the $\gamma\gamma$ + 2-jet processes at NLO in QCD,

$$pp \longrightarrow \gamma\gamma + 2 \text{ jets}\,. \tag{2.1}$$

These processes receive contributions from several partonic subprocesses. At leading order, and in the virtual NLO contributions, the subprocesses are all obtained from

$$\begin{aligned} q\bar{q}gg &\to \gamma\gamma\,, \\ q\bar{q}q'\bar{q}' &\to \gamma\gamma\,, \end{aligned} \tag{2.2}$$

by crossing two of the initial-state partons into the final state. We illustrate the virtual contributions with one or two external quark pairs in figs. 1–3, although we do not need any of the diagrams explicitly, as our calculation uses on-shell methods rather than Feynman diagrams. There are additional 'pure-gluon' scattering processes that we may consider,

$$gg \to \gamma\gamma gg\,, \tag{2.3}$$

which have no external quark legs. This process, illustrated in fig. 4, vanishes at tree level and appears only at one loop. Accordingly, the amplitude is finite at one loop, and it appears

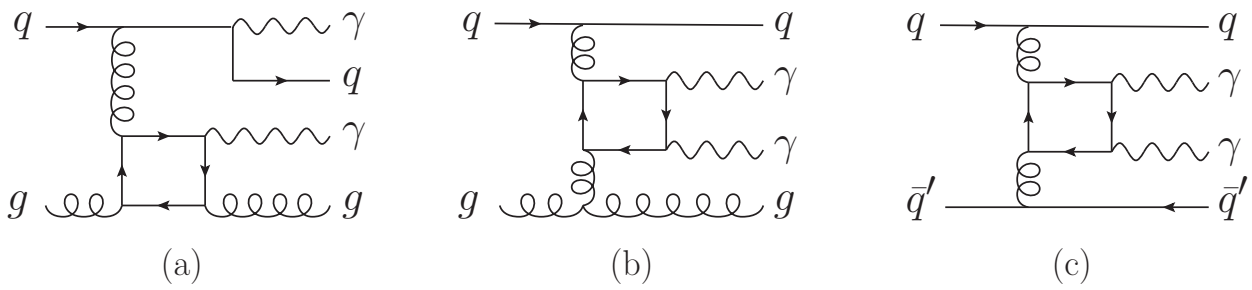

FIG. 3: Examples of six-point fermion-loop diagrams for the processes $qg \to \gamma\gamma qg$ and $q\bar{q}' \to \gamma\gamma q\bar{q}'$. These diagrams have a closed quark loop. In (a), one photon couples directly to the quark loop, whereas in (b) and (c), both photons couple to the quark loop.

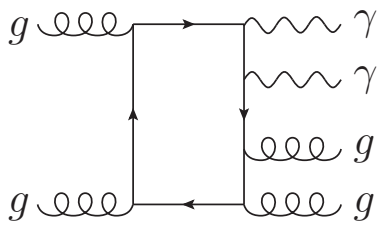

FIG. 4: Example of a six-point one-loop diagram for the process $gg \to \gamma\gamma gg$. This one-loop amplitude is finite because the corresponding tree-level amplitude vanishes.

in the squared matrix element only at relative order α_s^2, as a one-loop squared contribution. In $\gamma\gamma+$ 0-jet or $\gamma\gamma+$ 1-jet production, these processes contribute at a significant or noticeable level (respectively), because there is no tree-level process with a gg initial state. The large value of the gluon distribution can compensate for the additional two powers of α_s, so these subprocesses must be taken into account. In $\gamma\gamma+$ 2-jet production, in contrast, one crossing of the first subprocess in eq. (2.2), in which the quark pair is moved to the final state, does give a tree-level contribution with a gg initial state. We might then expect the contribution of the pure-gluon subprocess to be genuinely suppressed by two powers of α_s, relative to this other gg initial-state contribution (although it does have a different dependence on the quark electric charges). We shall test this expectation by including the matrix element for the $gg \to \gamma\gamma gg$ subprocess explicitly in the NLO calculation. While we will find that its contribution is small in the total, it is not as small compared to the tree-level gg initial-state contribution as this argument would suggest. (We do not include similar contributions from

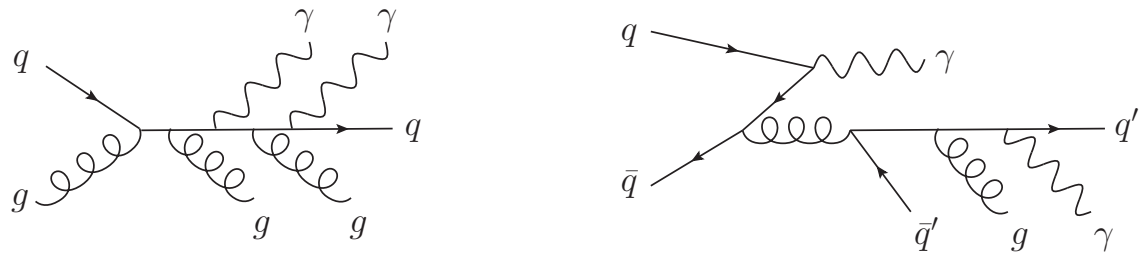

FIG. 5: Examples of seven-point real-emission diagrams for the processes $qg \to \gamma\gamma qggg$ and $q\bar{q} \to \gamma\gamma q'\bar{q}'g$.

the squaring of finite one-loop helicity amplitudes in the $gg \to \gamma\gamma q\bar{q}$ subprocess, which are expected to give smaller contributions.)

In our computation, we obtain amplitudes with multiple identical quark flavors by appropriate antisymmetrization of amplitudes for distinct flavors. The virtual contributions to any given subprocess can be divided into gauge-invariant subparts. For example, the contributions to amplitudes with a closed quark loop form a gauge-invariant subset. The quark-loop contributions can be split up further, depending on the lines to which the external photons couple. Terms in which neither photon couples to the closed quark loop, but only to the open quark lines (lines that connect to external states), as shown in fig. 2, give a contribution proportional to n_f, the number of quark flavors. Terms with one photon coupling to the closed quark loop and one to an open quark line, as shown in fig. 3(a), give a contribution proportional to the flavor sum of quark charges, $\sum_f Q_f$. Finally, terms in which both photons couple directly to the closed quark loop, as shown in fig. 3(b), give a contribution proportional to the flavor sum of squared quark charges, $\sum_f Q_f^2$. The pure-gluon subprocesses (2.3), shown in fig. 4, are likewise proportional to this latter flavor sum.

Calculations to NLO in QCD also require real-emission matrix elements, corresponding to contributions with an additional parton in the final state. We obtain the required subprocesses by crossing three initial-state partons into the final state in one of the two basic processes,

$$\begin{aligned} q\bar{q}ggg &\to \gamma\gamma\,, \\ q\bar{q}q'\bar{q}'g &\to \gamma\gamma\,. \end{aligned} \tag{2.4}$$

We illustrate these processes in fig. 5.

In our calculation, the five lightest quarks, u, d, c, s, b, are all treated as massless. We do

not include contributions to the amplitudes from real or virtual top quarks; we expect this omission to affect our results only at the percent level.

A. Photon Isolation

Photon measurements make use of an isolation criterion in order to suppress backgrounds from photons arising from hadrons. From an experimental point of view, the isolation requirement is necessary to reduce an important background, consisting of jets with a π^0 or η meson carrying most of the jet's energy, which is then misidentified as an isolated photon because it decays to a nearly-collinear photon pair. Experimental collaborations typically use an isolation criterion (see *e.g.* refs. [30, 31]), imposing a limit on the hadronic energy in a cone around the photon. This limit may be applied after subtractions to account for detector noise, the effects of the underlying event or of pile-up of other pp collisions, and possible adjustments for photon energy not captured within the cone. As a result, the hadronic energy within the cone may even be negative; along with the accounting for underlying event or pile-up activity, this weakens the link with a purely perturbative implementation of a fixed-cone isolation criterion.

A fixed-cone isolation criterion requires the use of nonperturbative photon fragmentation functions in order to obtain theoretical predictions. The use of fragmentation functions requires additional work, and in any case it would limit the precision attainable, because the fragmentation functions are not that well constrained by experimental data. Furthermore, unlike the case of the parton distribution functions, no error sets are available that would allow us to estimate the uncertainties due to the fragmentation functions. These issues weaken the motivation for using a fixed-cone isolation in a theoretical calculation, compared to possible alternative isolation procedures.

Frixione proposed such an alternative photon isolation procedure, which avoids the need for fragmentation-function contributions [32] by suppressing the region of phase space where photons are collinear with jets. It still allows soft radiation arbitrarily close to the photon, ensuring that it is infrared safe. We use this procedure, requiring that the partons obey,

$$\sum_i E_{\mathrm{T}i}\,\Theta\left(\delta - R_{i\gamma}\right) \leq E(\delta)\,, \tag{2.5}$$

for all $\delta = R(\phi, \eta; \phi_\gamma, \eta_\gamma) \leq \delta_0$, where

$$R(\phi_1, \eta_1; \phi_2, \eta_2) = [(\phi_1 - \phi_2)^2 + (\eta_1 - \eta_2)^2]^{1/2}\,, \tag{2.6}$$

is the usual longitudinally boost-invariant angular distance measure. In the inequality (2.5), $R_{i\gamma} = R(\phi_i, \eta_i; \phi_\gamma, \eta_\gamma)$ is the distance of parton i from the photon, $E_{\mathrm{T}i}$ is the transverse energy of the ith parton and the restricting function $E(\delta)$ is given by

$$E(\delta) = E_{\mathrm{T}}^{\gamma}\, \epsilon_\gamma \left(\frac{1 - \cos\delta}{1 - \cos\delta_0} \right)^n . \tag{2.7}$$

The restriction is scaled by the parameter ϵ_γ to the photon transverse energy E_{T}^{γ}. The inequality (2.5) constrains the hadronic energy in a cone of fixed half-angle δ_0 around the photon axis. The restricting function has the property that it vanishes as $\delta \to 0$ and thus suppresses collinear configurations, but allows soft radiation arbitrarily close to the photon. We will use the Frixione cone, with,

$$\epsilon_\gamma = 0.5\,, \quad \delta_0 = 0.4\,, \quad \text{and} \quad n = 1\,. \tag{2.8}$$

An earlier study [20] of inclusive photon production found that the difference in cross sections between Frixione cone and fixed-cone isolation, with similar parameters to the present study, was less than 1% at large photon transverse momenta. Although the Frixione isolation has not been applied directly in experiments, here at least, we do not expect the discrepancy to be large.

Our implementation follows the standard SHERPA one; the photon isolation and jet algorithm using the FastJet [33] library are applied independently, with no special treatment for partons inside the photon cone. After isolation and jet-finding, we apply an additional angular separation criterion to photon–jet pairs and to the pair of photons.

B. Formalism and Software

Several ingredients enter into an NLO calculation: the Born cross section, the virtual (one-loop) corrections, and the radiative (real-emission) corrections. The computation of the latter requires tree-level matrix elements with an additional parton in the final state compared to the Born process. The virtual corrections have explicit divergences in the dimensional regulator $\epsilon = (4-D)/2$, whereas the canceling divergences in the real-emission contributions

arise only after integration over D-dimensional phase space. We use the Catani–Seymour dipole subtraction scheme [28] in order to implement these cancellations in a numerical calculation. This scheme adds and subtracts contributions to the evaluation of the NLO cross section; schematically, we decompose it as,

$$\sigma_n^{\rm NLO} \;=\; \int_n \sigma_n^{\rm born} \;+\; \int_n \sigma_n^{\rm virt} \;+\; \int_n \Sigma_n^{\rm subtr} \;+\; \int_{n+1} \left(\sigma_{n+1}^{\rm real} \;-\; \sigma_{n+1}^{\rm subtr}\right) . \tag{2.9}$$

Here the subscripts on the integrals denote the number of final-state partons, and $\Sigma_n^{\rm subtr}$ is the result of integrating $\sigma_{n+1}^{\rm subtr}$ analytically over a one-particle unresolved phase space. Other subtraction methods in current use include the FKS approach [34] and antenna subtraction [35]; the former has been automated [36]. We use the SHERPA package [12] to manage the partonic subprocesses, to integrate over phase space, and to output ROOT [26] n-tuples.

The techniques we use for computing virtual contributions are collectively known as on-shell methods, and are reviewed in refs. [37]. These methods rely on underlying properties of amplitudes — factorization and unitarity — in order to express them in terms of simpler, on-shell amplitudes of lower multiplicity, reducing the swell of terms. Early application of the unitarity method [38] to collider physics was to computing analytically the one-loop matrix elements for $q\bar{q}ggg$, $q\bar{q}ggV$ and $q\bar{q}q'\bar{q}'V$ ($V = W$ or Z) processes [39]. The latter matrix elements are used, for example, in the NLO program MCFM [40] as well as in studies at e^+e^- colliders. In recent years, on-shell methods have been implemented in a more flexible numerical form. These methods scale well as the number of external legs increases [13, 16, 17, 24, 25, 41–46]. There have also been important advances in computing virtual corrections with more traditional methods [47, 48].

One-loop amplitudes in QCD with massless quarks may be expressed as a sum over three different types of Feynman integrals (boxes, triangles, and bubbles) with additional 'rational' terms. These latter terms are rational functions of spinor variables associated to the external momenta. The integrals' coefficients are also rational functions of these variables. The integrals are universal and well-tabulated; the aim of the calculation is to compute their coefficients as well as the rational terms. In an on-shell approach, the integral coefficients may be computed using four-dimensional generalized unitarity [38, 39, 49], while the rational terms may be computed either by a loop-level version [41] of on-shell recursion [50] or using D-dimensional unitarity [51]. We use a numerical version [11] of Forde's method [52] for

the integral coefficients, and subtract box and triangle integrands along the lines of the Ossola–Papadopoulos–Pittau procedure [53], improving the numerical stability. To compute the rational terms, we use a numerical implementation of Badger's massive continuation method [54], which is related to D-dimensional unitarity.

These algorithms are implemented in the BlackHat software library [11, 44]. BlackHat organizes the computation of the amplitudes in terms of elementary gauge-invariant "primitive amplitude" building blocks [39, 55]. The primitive amplitudes are then assembled into partial amplitudes, which are the kinematic coefficients of the different color tensors that can appear in the amplitude. The complete virtual cross section is obtained by interfering the one-loop partial amplitudes with the tree-level amplitude and summing over spins and color indices. A given primitive amplitude can appear in multiple partial amplitudes and does not have to be recomputed for each one.

This approach also allows for a straightforward separation of leading- and subleading-color contributions. The subleading-color contributions are much smaller, yet more computationally costly (10 times slower per phase-space point for $\gamma\gamma$ + 2-jet production), but using the separation we can evaluate them at far fewer phase-space points than the leading-color contributions, while obtaining comparable absolute statistical uncertainties. Similarly to the production of a W boson in association with three [13] or four jets [56], the subleading-color terms in the virtual contributions are small. The magnitude of these subleading-color contributions depends strongly on the cuts. With standard cuts, they are typically 2% of the leading-color virtual terms, and about 0.2% of the cross section. With VBF cuts applied in addition, these percentages increase to 5% of the virtual, and 2% of the cross section. Our results are based on event samples of $7 \cdot 10^6$ leading-color virtual events, and $6 \cdot 10^5$ subleading color ones.

As explained earlier in this section, there are four distinct types of contributions to an NLO calculation: Born, virtual, integrated-subtraction, and subtracted real-emission. We perform the phase-space integration of each type independently, using adaptive Monte-Carlo integration [57]. We use an efficient hierarchical phase-space generator based on QCD antenna structures [58], as incorporated into SHERPA [27]. For each integration, the code adapts a grid during an initial phase; the grid is then frozen, and used in the next, high-statistics phase, which provides an estimate of the integration result and associated statistical uncertainties. SHERPA's integrator adjusts the relative number of evaluations between dif-

ferent subprocesses during grid generation, in order to optimize the statistical uncertainties of the computed cross section with a fixed number of matrix-element evaluations.

For the virtual contributions, we use the associated Born matrix elements to adapt and refine the integration grid. For the pure-gluon terms, we cannot do this, because the corresponding tree-level amplitudes vanish identically; instead, we use antenna functions for this purpose. The choice of the antenna functions is somewhat arbitrary, but the choice will affect only how quickly the final phase-space integration converges, and not the result itself. We choose the antenna functions to incorporate most of the singularities present in the one-loop amplitudes squared. As an example, consider the integration of the squared matrix element $M\bigl(g_1, g_2, g_3, \gamma_4, \gamma_5\bigr)$ in more detail. We compute an antenna function using a combination of color-ordered gluon tree amplitudes symmetrized over g_4 and g_5: $A^{\rm sym} \equiv (A^{\rm tree}\bigl(g_1, g_2, g_3, g_4, g_5\bigr) + A^{\rm tree}\bigl(g_1, g_2, g_3, g_5, g_4\bigr))$. The antenna function is then the squared matrix element $|A^{\rm sym}|^2$, summed over colors and helicities.

The NLO result also requires real-emission corrections to the LO process, which arise from tree-level amplitudes with one additional parton; illustrative diagrams are shown in fig. 5. We use the COMIX library [27], included in the SHERPA framework [12], to compute these contributions, including the Catani–Seymour dipole subtraction terms [28]. The COMIX code is based on a color-dressed form [59] of the Berends-Giele recursion relations [60], making it very efficient for processes with high multiplicities.

In the results described in the present article, we restrict attention to one PDF set, and one jet algorithm. We do use several correlated values of the renormalization and factorization scales in order to estimate the scale-dependence bands at LO and at NLO. In addition, we study several different choices for the experimental cuts. In general, however, we might need to compute the same physical distributions for a collection of PDF error sets, and for different jet algorithms, in addition to different renormalization and factorization scales. We organize the computation so that the matrix elements do not have to be reevaluated anew for each choice of PDF, of scales, or of jet-algorithm parameters (within a limited set) [29]. We do this by storing intermediate information in ROOT-format n-tuple files [26]. This format has also been used by the experimental collaborations to compare results from BlackHat + SHERPA to experimental data [23].

C. Checks

We have performed a number of consistency checks on the virtual amplitudes and on integrated cross sections. We have checked the factorization properties of primitive amplitudes. As checks on our diphoton setup, at isolated phase-space points, we have checked the $gg\gamma\gamma$ amplitude against MCFM [40]; the $q\bar{q}\gamma\gamma$ amplitude against HELAC-1LOOP [61]; the $ggg\gamma\gamma$ amplitude against GoSam [25]; the $q\bar{q}g\gamma\gamma$ amplitude against older analytic results obtained from various permutations of the $q\bar{q}ggg$ amplitudes in ref. [55] and against GoSam; and a selection of $\gamma\gamma$ + 2-jet amplitudes against GoSam. We have also compared the cross section for $\gamma\gamma$ + 0-jet production with MCFM, that for $\gamma\gamma$ + 1-jet production with the results of Gehrmann, Greiner and Heinrich (GGH) [8], and that for $\gamma\gamma$ + 2-jet production with the GGH results [9]. When we use their cuts and choice of central scale, we find agreement for the total cross section.

D. Kinematics and Observables

In our study, we consider the inclusive process $pp \to \gamma\gamma + 2$ jets at an LHC center-of-mass energy of $\sqrt{s} = 8$ TeV, applying the following cuts:

$$\begin{aligned} &p_{\rm T}^{\gamma_1} > 50 \text{ GeV}\,, && p_{\rm T}^{\gamma_2} > 25 \text{ GeV}\,, && |\eta_\gamma| < 2.5\,, && R_{\gamma\gamma} > 0.45\,, \\ &p_{\rm T}^{\rm jet_1} > 40 \text{ GeV}\,, && p_{\rm T}^{\rm jet_2} > 25 \text{ GeV}\,, && |\eta_{\rm jet}| < 4.5\,, && R_{\gamma,\rm jet} > 0.4\,. \end{aligned} \tag{2.10}$$

We will call these the 'basic' set of cuts. In these expressions, R is the usual longitudinally boost-invariant angular distance, $R_{ab} = [\Delta\phi_{ab}^2 + \Delta\eta_{ab}^2]^{1/2}$. We define jets using the anti-k_T algorithm [62] with parameter $R = 0.4$. The jets are ordered in transverse momentum $p_{\rm T}$, and are labeled numerically in order of decreasing $p_{\rm T}$, with jet 1 being the leading (hardest) jet.

In addition, we also consider further cuts, which select the kinematic region for VBF production of the Higgs-like boson, with the boson decaying into two photons. We will call these the VBF cuts,

$$M_{jj} > 400 \text{ GeV}\,, \qquad |\Delta\eta_{jj}| > 2.8\,, \tag{2.11}$$

where M_{jj} is the invariant mass of the subsystem made up of the two hardest jets, and $\Delta\eta_{jj}$ is the difference in pseudorapidity between these two jets. We will show distributions both with and without VBF cuts.

For the central renormalization and factorization scale in our calculation, we use the dynamical scale $\hat{H}_{\rm T}/2$, where

$$\hat{H}_{\rm T} \equiv p_{\rm T}^{\gamma_1} + p_{\rm T}^{\gamma_2} + \sum_m p_{\rm T}^m \,. \tag{2.12}$$

The sum runs over all final-state partons m, whether or not they are inside jets that pass the cuts. This means that modifications to the experimental cuts will not affect the value of the matrix element at a given point in phase space. We note in passing that because the photons are massless, $\hat{H}_{\rm T}$ in this calculation has the same value as the $\hat{H}'_{\rm T}$ variable the BlackHat collaboration has employed previously for studies of W or Z production accompanied by jets. (In $\hat{H}'_{\rm T}$, the transverse momentum of a boson with mass M is replaced by the transverse energy $E_{\rm T} = \sqrt{p_{\rm T}^2 + M^2}$.) We quote scale variation bands corresponding to varying the scales simultaneously up and down by a factor of two, taking the maximum and minimum of differential cross sections at the five scales $\hat{H}_{\rm T}/2 \times (1/2, 1/\sqrt{2}, 1, \sqrt{2}, 2)$.

We also study the effect of an additional set of cuts, suggested by the ATLAS collaboration, which selects a window on the diphoton invariant mass centered around the Higgs-like boson mass,

$$\begin{aligned}
&122 \text{ GeV} \leq m_{\gamma\gamma} \leq 130 \text{ GeV}\,, \\
&p_{\rm T}^{\gamma_1} > 0.35\, m_{\gamma\gamma}\,, \qquad p_{\rm T}^{\gamma_2} > 0.25\, m_{\gamma\gamma}\,, \qquad |y_\gamma| < 2.37\,, \qquad R_{\gamma\gamma} > 0.45\,, \\
&p_{\rm T}^{\rm jet} > 30 \text{ GeV}\,, \qquad R_{\gamma,\rm jet} > 0.4\,, \qquad |y_{\rm jet}| < 4.4\,.
\end{aligned} \tag{2.13}$$

We will call these the 'ATLAS' cuts. The additional VBF cuts here are the same as those in eq. (2.11).

Finally, we study a set of cuts suggested by the CMS collaboration,

$$\begin{aligned}
&100 \text{ GeV} \leq m_{\gamma\gamma} \leq 180 \text{ GeV}\,, \\
&p_{\rm T}^{\gamma_1} > m_{\gamma\gamma}/2\,, \qquad p_{\rm T}^{\gamma_2} > 25\,\text{GeV}\,, \qquad |\eta_\gamma| < 2.5\,, \\
&p_{\rm T}^{\rm jet} > 30\,\text{GeV}\,, \qquad R_{\gamma\gamma} > 0.45\,, \qquad |\eta_{\rm jet}| < 4.7\,, \\
&R_{\gamma,\rm jet} > 0.5\,, \qquad |\phi_{jj} - \phi_{\gamma\gamma}| > 2.6\,, \qquad |\eta^*| < 2.5\,.
\end{aligned} \tag{2.14}$$

In these inequalities, ϕ_{jj} and $\phi_{\gamma\gamma}$ denote the azimuthal angle of the dijet and diphoton systems, respectively. and η^* denotes the relative diphoton pseudorapidity (as introduced by Rainwater, Szalapski, and Zeppenfeld [63]),

$$\eta^* = \eta_{\gamma\gamma} - \frac{1}{2}(\eta_{\rm jet_1} + \eta_{\rm jet_2})\,. \tag{2.15}$$

In this equation, the pseudorapidity $\eta_{\gamma\gamma} = -\ln\tan(\theta_{\gamma\gamma}/2)$, where $\theta_{\gamma\gamma}$ is the polar angle in the lab frame for the diphoton momentum vector. The jet algorithm used here is anti-$k_{\rm T}$ with $R = 0.5$. We will call these the 'CMS' cuts.

The additional VBF cuts in this case are,

$$M_{jj} > 500\,\text{GeV}\,, \qquad |\Delta\eta_{jj}| > 3\,. \tag{2.16}$$

The calculation proceeds in two phases: generation of n-tuples, and analysis. In the first phase, we generate two sets of ROOT [26] format n-tuples using a looser set of cuts,

$$\begin{aligned} &p_{\rm T}^{\gamma_1} > 25\ \text{GeV}\,, \qquad p_{\rm T}^{\gamma_2} > 25\ \text{GeV}\,, \qquad |\eta_\gamma| < 2.5\,, \qquad R_{\gamma\gamma} > 0.2\,, \\ &p_{\rm T}^{\text{jet}_1} > 25\ \text{GeV}\,, \qquad p_{\rm T}^{\text{jet}_2} > 25\ \text{GeV}\,, \qquad |\eta_{\rm jet}| < 4.8\,, \qquad R_{\gamma,\rm jet} > 0.4\,, \end{aligned} \tag{2.17}$$

where the $R_{\gamma,\rm jet}$ cut at generation level is applied only to the leading two jets, with the second set also imposing VBF cuts that are looser than those of eq. (2.11),

$$M_{jj} > 300\ \text{GeV}\,, \qquad |\Delta\eta_{jj}| > 2.0\,. \tag{2.18}$$

In principle, if we had sufficient statistics in the first set, generated with the cuts of eq. (2.17), we would not need a second, more targeted set, in order to study the effect of VBF cuts. These cuts push us into a small corner of phase space, however, reducing the cross section by a factor of roughly 20. Adequate statistics in the first set would thus be 400 times larger than would be needed for studies without VBF cuts. It is much more efficient to generate a second set of n-tuples in order to obtain reasonable statistical uncertainties for the latter cuts. The first set of n-tuples are in the process directory `YY2j`, and the second in `YY2j_VBF`. The location of the directory may be found in `http://blackhat.hepforge.org/trac/wiki/Location`.

In the second, analysis, phase of our calculation we impose the following six sets of cuts:

Basic:	cuts of eq. (2.10)
Basic+VBF:	cuts of eq. (2.10) and eq. (2.11)
ATLAS:	cuts of eq. (2.13)
ATLAS VBF:	cuts of eq. (2.13) and eq. (2.11)
CMS:	cuts of eq. (2.14)
CMS VBF:	cuts of eq. (2.14) and eq. (2.16)

We compute the cross section for each set of cuts, as well as various kinematical distributions.

The n-tuples we have generated are also valid for anti-k_T, k_T and SISCone algorithms [62, 64] for $R = 0.4, 0.5, 0.6, 0.7$, as implemented in the FASTJET package [33]. In the SISCone case the merging parameter f is chosen to be 0.75.

In addition to distributions in transverse momenta, invariant masses, rapidities, and azimuthal angles, we will also study a distribution in $\cos\theta^*$, the cosine of the polar angle of the photon pair with respect to the z axis of the Collins–Soper frame [65]. This variable can also be expressed as,

$$|\cos\theta^*| \;=\; \frac{|\sinh(\Delta\eta_{\gamma\gamma})|}{\sqrt{1+(p_{\rm T}^{\gamma\gamma}/m_{\gamma\gamma})^2}}\frac{2p_{\rm T}^{\gamma_1}p_{\rm T}^{\gamma_2}}{m_{\gamma\gamma}^2}\,. \tag{2.19}$$

It has been used by the ATLAS [66] and CMS [67] collaborations in their studies of the diphoton decays of the Higgs-like boson.

In our study, we use the MSTW2008 LO and NLO PDFs [68] at the respective orders. We use the five-flavor running $\alpha_s(\mu)$ and the value of $\alpha_s(M_Z)$ supplied with the parton distribution functions. As explained in ref. [20] (see also refs. [69]), we use the zero-momentum-squared value, $\alpha_{\rm EM}(0) = 1/137$ (to our required precision), for the electromagnetic coupling.

We perform our fixed-order NLO computation at the parton level. We do not apply a parton shower, or corrections due to non-perturbative effects such as those induced by the underlying event or hadronization. For comparisons to experiment it is important to incorporate these effects or at least estimate their size.

III. RESULTS

A. Scale dependence

We expect perturbative results to be more stable under variation of the renormalization and factorization scales as the perturbative order is increased. The residual variability has been used as a proxy for the expected uncertainty due to higher-order corrections beyond the calculated order. As an example, we saw that in studies of W in association with several jets [13, 14, 16, 18], the variability increases substantially with a growing number of jets at LO, but stabilizes at under 20% at NLO (for a range of scales between half and twice the central value). In fig. 6, we show how the cross section for $\gamma\gamma$ + 2-jet production varies with a common renormalization and factorization scale, $\mu_R = \mu_F = \mu$. We vary the common

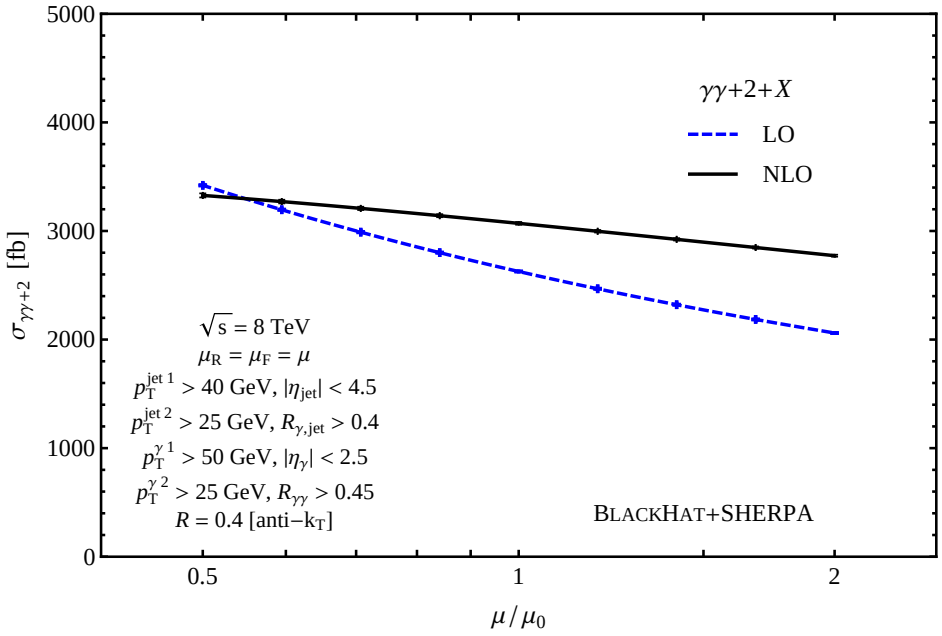

FIG. 6: The renormalization-scale dependence of the cross section for $\gamma\gamma$ + 2-jet production using a dynamical central scale of $\mu_0 = \hat{H}_T/2$. The renormalization and factorization scales are kept equal and varied simultaneously. The LO result is given by the dashed (blue) line, and the NLO one by the solid (black) line. The error bars indicate the numerical integration uncertainties.

scale up and down by a factor of 2 at both LO and NLO, around a central choice of $\hat{H}_T/2$. The NLO variation is under 10% of the central value.

The kinematical distributions we study have a large dynamic range, and $\hat{H}_T/2$ is a suitable event-by-event scale, matching typical energy scales individually rather than merely on average. In section III C, we plot a variety of distributions. The bands in the plots all correspond to varying the scales up and down by a factor of 2 around the central value. Other authors have suggested alternate choices of dynamical scale [48, 70]; GGH have used such an alternate dynamical scale [9].

B. Dependence on the Frixione-Cone Energy Fraction

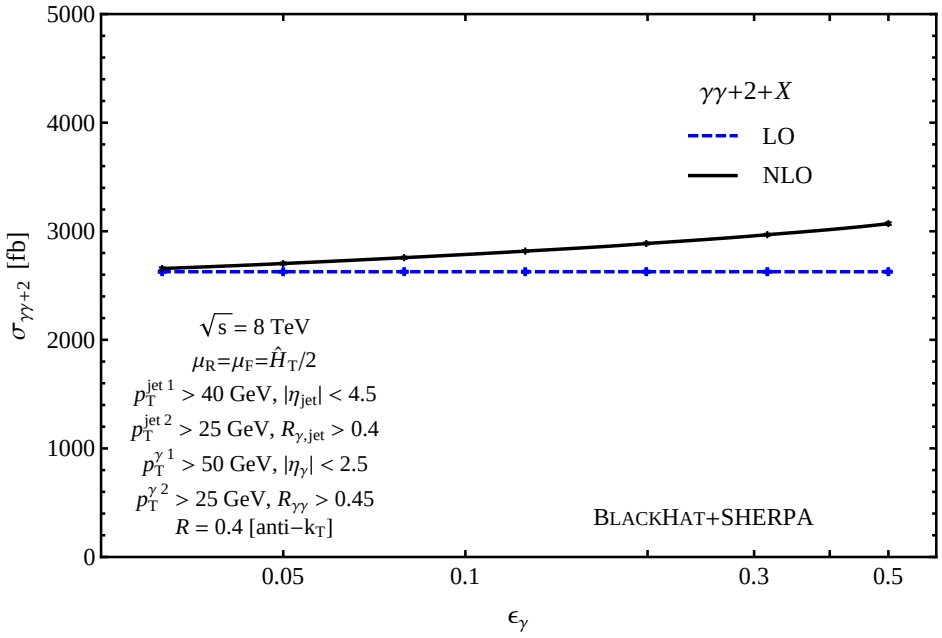

FIG. 7: The dependence of the cross section on the ϵ_γ parameter in the Frixione-cone photon isolation. The LO result is given by the dashed (blue) line, and the NLO one by the solid (black) line. The error bars indicate the numerical integration uncertainties.

In a previous study of single-photon production in association with jets, we observed that the NLO cross section depended only weakly on the parameters used for the Frixione-cone isolation of the photons. We have examined the dependence on one of these parameters, the energy fraction ϵ_γ, in the present study. The results are shown in fig. 7. The LO result is of course independent of the parameter, as there is no additional radiation that could enter the photon cone; this result is shown for comparison in the figure. The NLO cross section is only weakly dependent on this parameter in the range $0.03 < \epsilon_\gamma < 0.5$.

C. Cross Sections and Distributions

In Table I, we present the LO and NLO parton-level cross sections for inclusive diphoton production accompanied by two jets. We consider the six different sets of cuts discussed in section II D. We list separately the contributions from the $gg \to \gamma\gamma gg$ subprocess (this contribution is also included in the NLO prediction).

The pure-gluon process starts only at one loop, and is therefore suppressed by two powers of α_s. As discussed earlier, we might expect it to be genuinely suppressed compared to the

Cuts	LO	NLO	$gg \to \gamma\gamma gg$
Basic	$2627(3)^{+794}_{-567}$	$3070(13)^{+257}_{-298}$	48(3)
Basic+VBF	$136.0(0.2)^{+52.6}_{-34.9}$	$155(1)^{+14}_{-18}$	2.75(0.05)
ATLAS	$89.3(0.5)^{+26.6}_{-19.1}$	$100(2)^{+7}_{-9}$	1.46(0.05)
ATLAS+VBF	$3.91(0.03)^{+1.53}_{-1.01}$	$4.6(0.1)^{+0.5}_{-0.6}$	0.075(0.004)
CMS	$574(1)^{+170}_{-122}$	$596(3)^{+21}_{-43}$	7.82(0.08)
CMS+VBF	$11.84(0.05)^{+4.68}_{-3.09}$	$14.7(0.2)^{+2.0}_{-2.0}$	0.34(0.01)

TABLE I: Total cross sections in femtobarns for $\gamma\gamma$ + 2-jet production with various sets of cuts: basic (eq. (2.10)), VBF (eqs. (2.10) and (2.11)), ATLAS (eq. (2.13)), ATLAS VBF (eqs. (2.13) and (2.11)), CMS (eq. (2.14)), and CMS VBF (eqs. (2.14) and (2.16)). The numerical integration uncertainty is given in parentheses, and the scale dependence is quoted in superscripts and subscripts. The contribution of the $gg \to \gamma\gamma gg$ subprocess, shown separately in the last column, is small but is included in the NLO value.

tree-level gg initial-state contribution. We find that the pure-gluon subprocess does give only a small contribution, as shown in Table I: it contributes less than 2.5% of the NLO result in all cases. However, it is not as suppressed as one might have naively expected, compared to the LO gg initial-state contribution, which is approximately 5% of the LO cross section for both Basic and Basic+VBF cuts.

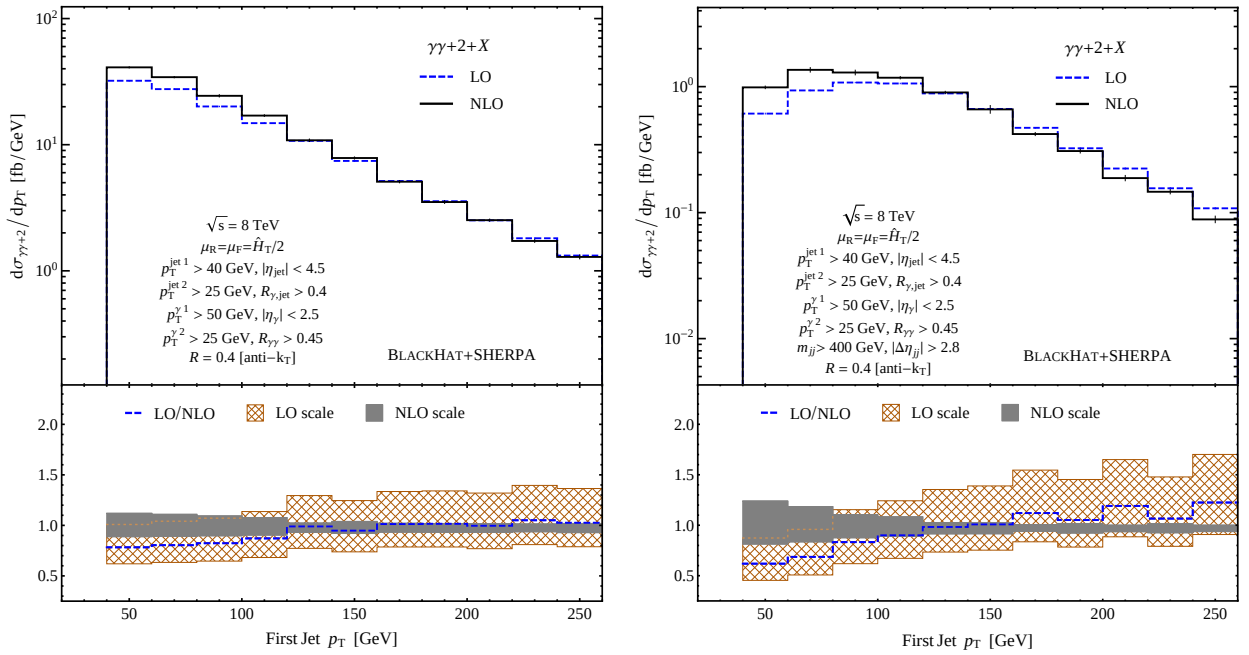

FIG. 8: The leading-jet transverse-momentum distribution in $\gamma\gamma$ + 2-jet production. The left plot shows the distribution for the basic cuts of eq. (2.10), and the right plot with the VBF cuts of eq. (2.11) in addition. The upper panels show the LO (dashed blue) and NLO (solid black) distributions, while the lower panels show the ratios to the NLO prediction, including the LO (hatched brown) and NLO (gray) scale-dependence bands. The thin vertical lines at the center of each bin (where visible) indicate the numerical integration errors for the bin.

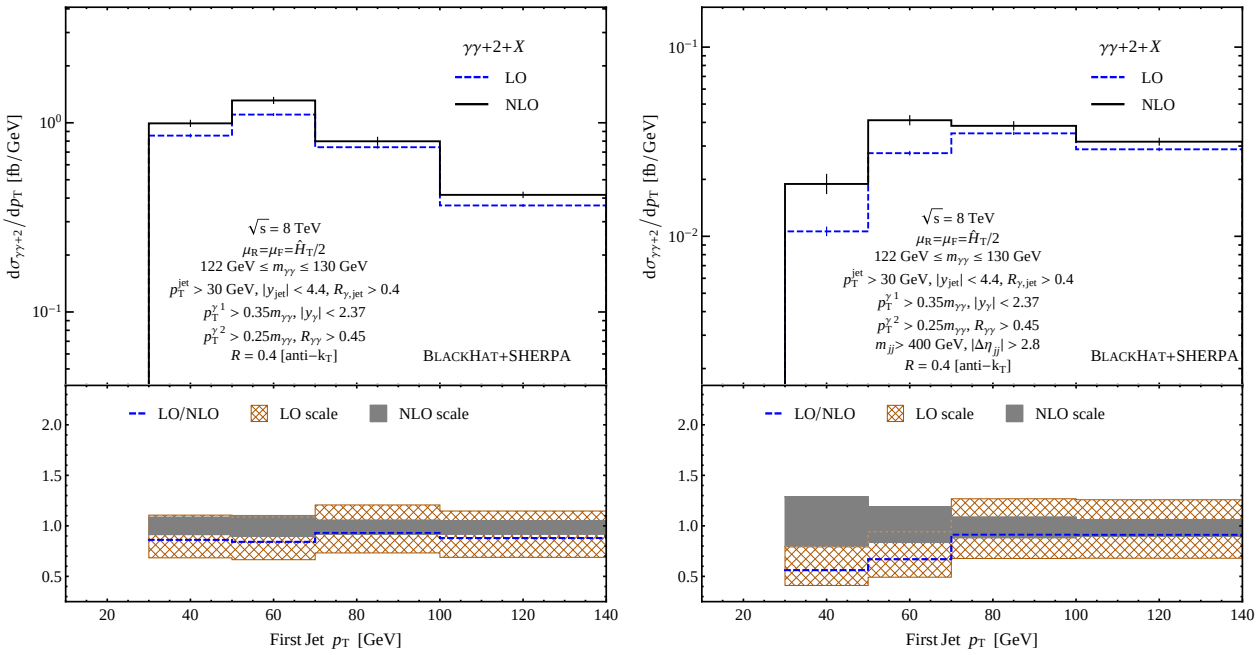

FIG. 9: The leading-jet transverse-momentum distribution in $\gamma\gamma$ + 2-jet production. The left plot shows the distribution for the ATLAS cuts of eq. (2.13), and the right plot with the VBF cuts of eq. (2.11) in addition. The panels, curves, and bands are as in fig. 8.

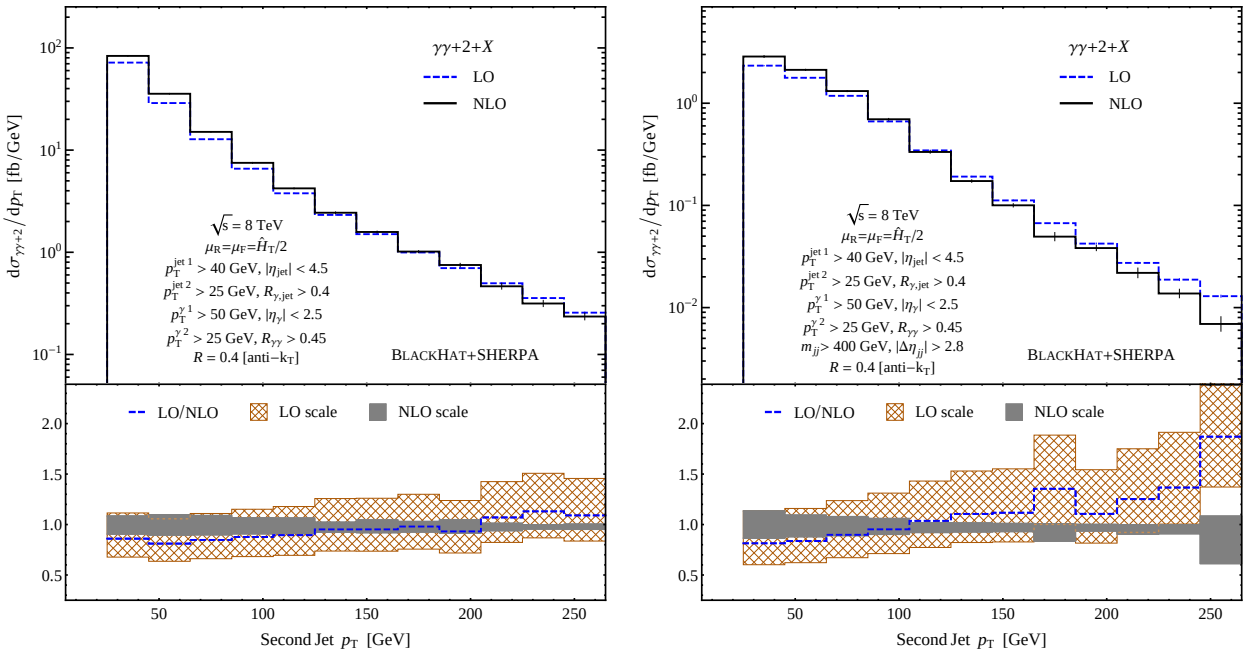

FIG. 10: The second jet transverse-momentum distribution in $\gamma\gamma + 2$-jet production. The left plot shows the distribution for the basic cuts of eq. (2.10), and the right plot with the VBF cuts of eq. (2.11) in addition. The panels, curves, and bands are as in fig. 8.

We also present predictions for a number of distributions. In fig. 8, we show the distribution in the transverse momentum of the leading jet for the cuts of eq. (2.10), and also with the addition of the VBF cuts of eq. (2.11). In fig. 9, we show the same distribution with the ATLAS cuts of eq. (2.13) as well as with the additional VBF cuts of eq. (2.11). We provide detailed tables of our results in appendices A, B, and C.

In figs. 10–13, we show a series of distributions side-by-side for the cuts of eq. (2.10) and for the same cuts with the addition of the VBF cuts of eq. (2.11): in fig. 10, the transverse momentum of the second jet; in fig. 11, the transverse momentum of the leading photon; in fig. 12, the dijet invariant mass; and in fig. 13, the photon-pair invariant mass.

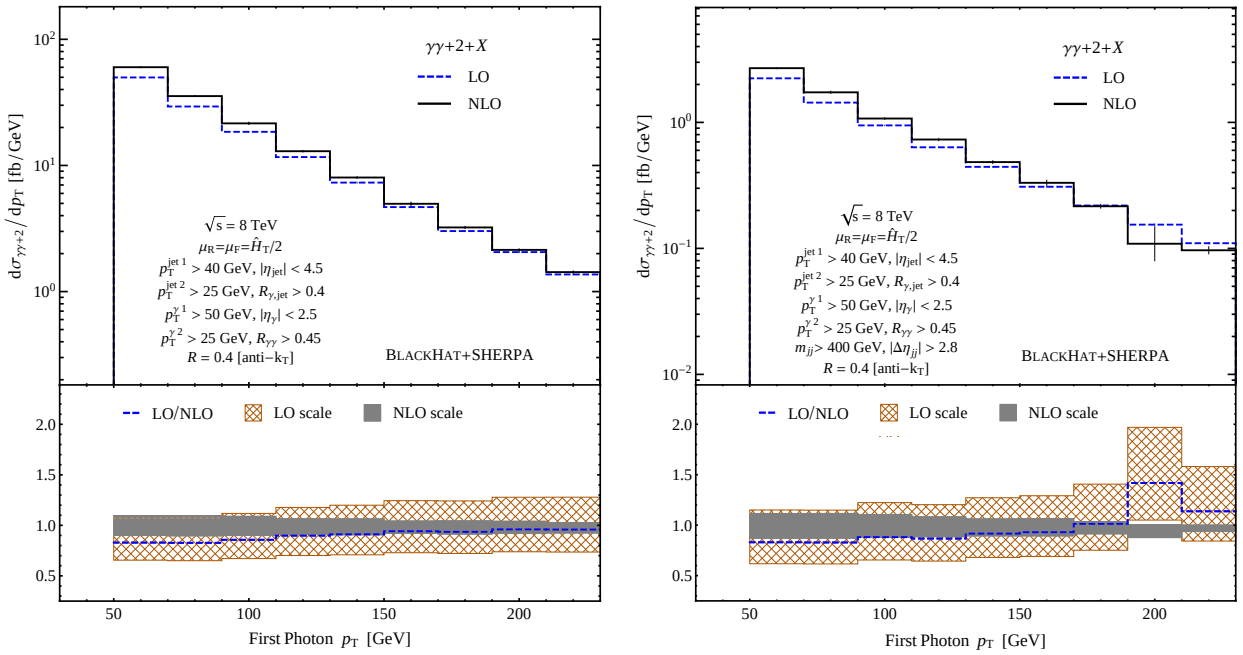

FIG. 11: The leading-photon transverse-momentum distribution in $\gamma\gamma$ + 2-jet production. The left plot shows the distribution for the basic cuts of eq. (2.10), and the right plot with the VBF cuts of eq. (2.11) in addition. The panels, curves, and bands are as in fig. 8.

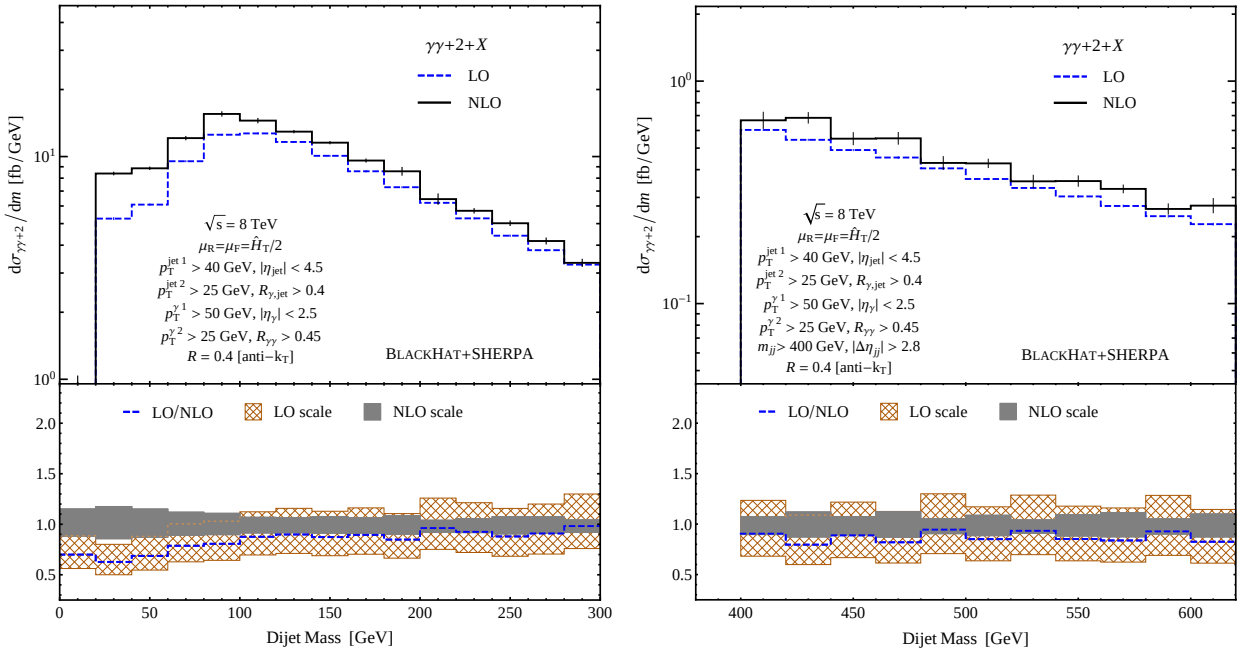

FIG. 12: The dijet invariant-mass distribution in $\gamma\gamma$ + 2-jet production. The left plot shows the distribution for the basic cuts of eq. (2.10), and the right plot with the VBF cuts of eq. (2.11) in addition. The panels, curves, and bands are as in fig. 8.

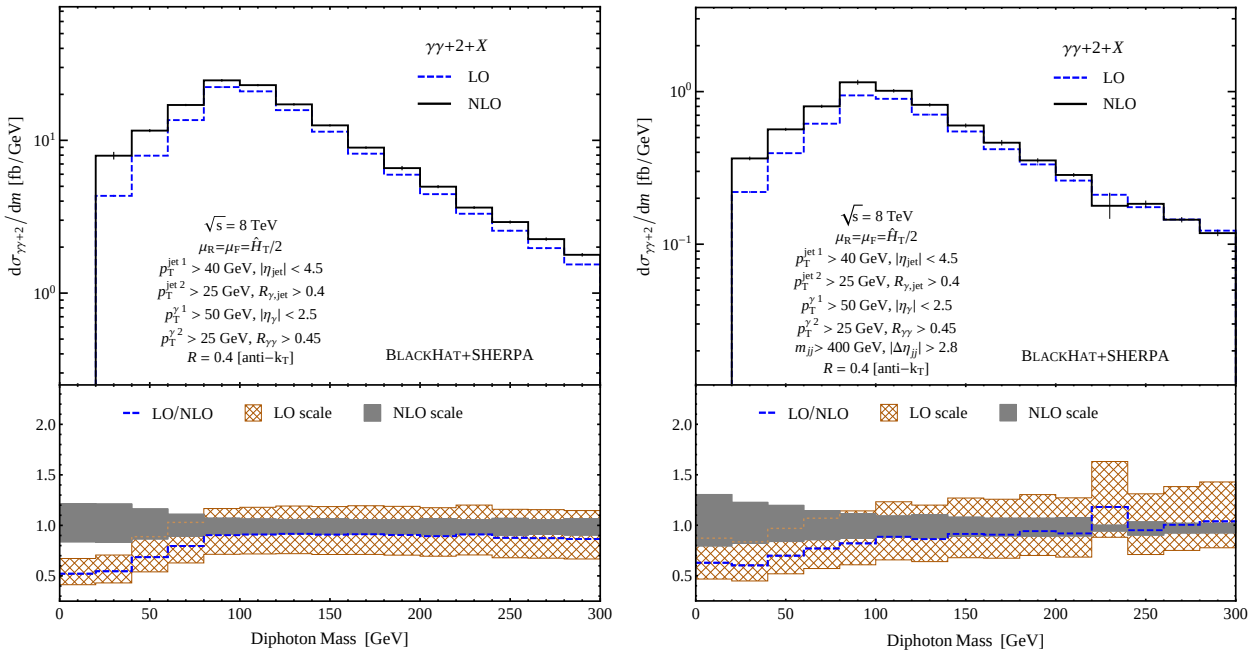

FIG. 13: The photon-pair invariant-mass distribution in $\gamma\gamma+$ 2-jet production. The left plot shows the distribution for the basic cuts of eq. (2.10), and the right plot with the VBF cuts of eq. (2.11) in addition. The panels, curves, and bands are as in fig. 8.

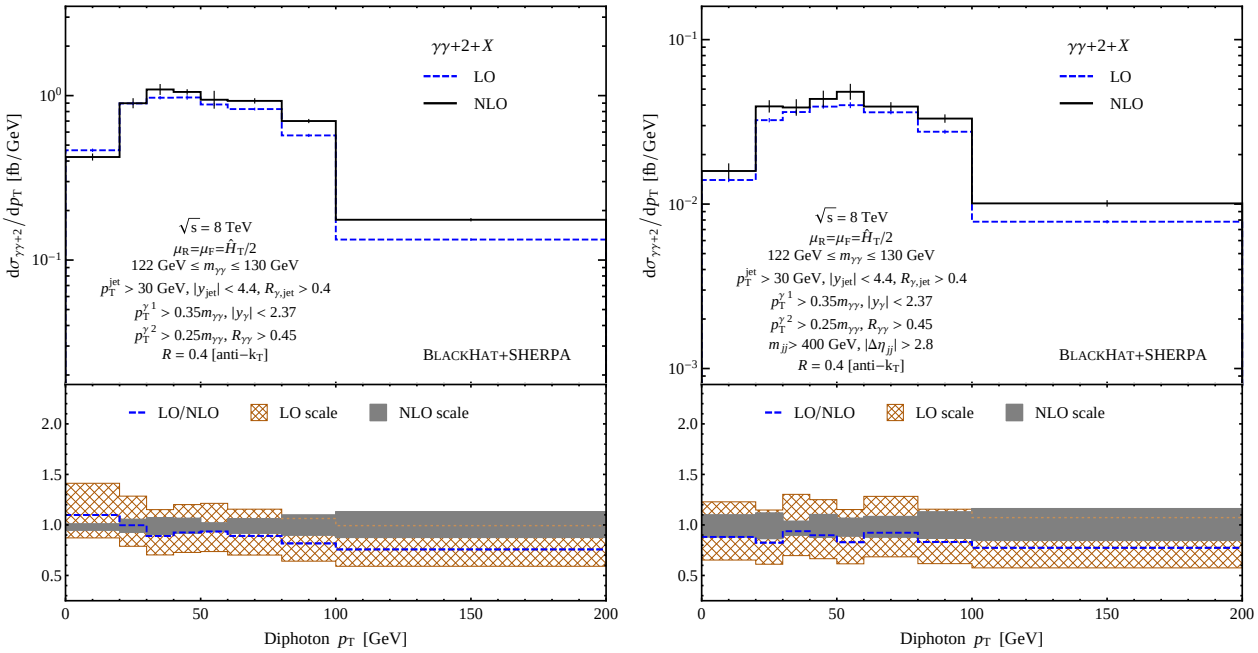

FIG. 14: The diphoton transverse-momentum distribution in $\gamma\gamma$ + 2-jet production. The left plot shows the distribution for the ATLAS cuts of eq. (2.13), and the right plot with the VBF cuts of eq. (2.11) in addition. The panels, curves, and bands are as in fig. 8.

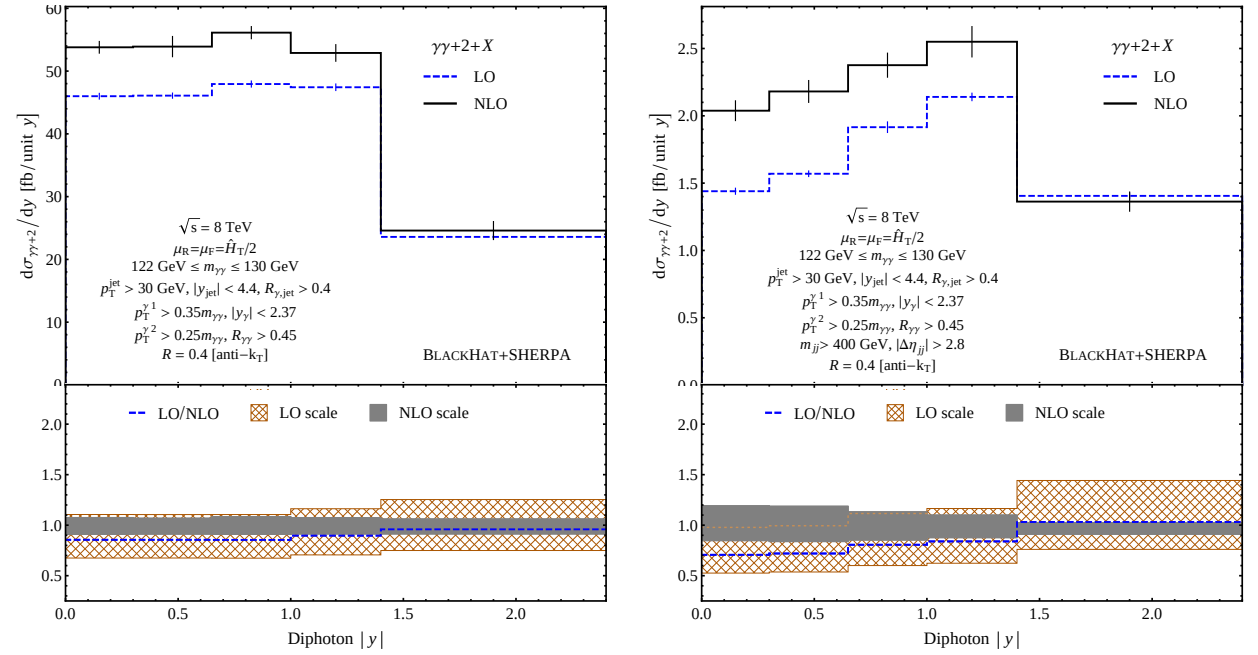

FIG. 15: The distribution of the absolute value of the diphoton rapidity in $\gamma\gamma$ + 2-jet production. The left plot shows the distribution for the ATLAS cuts of eq. (2.13), and the right plot with the VBF cuts of eq. (2.11) in addition. The panels, curves, and bands are as in fig. 8.

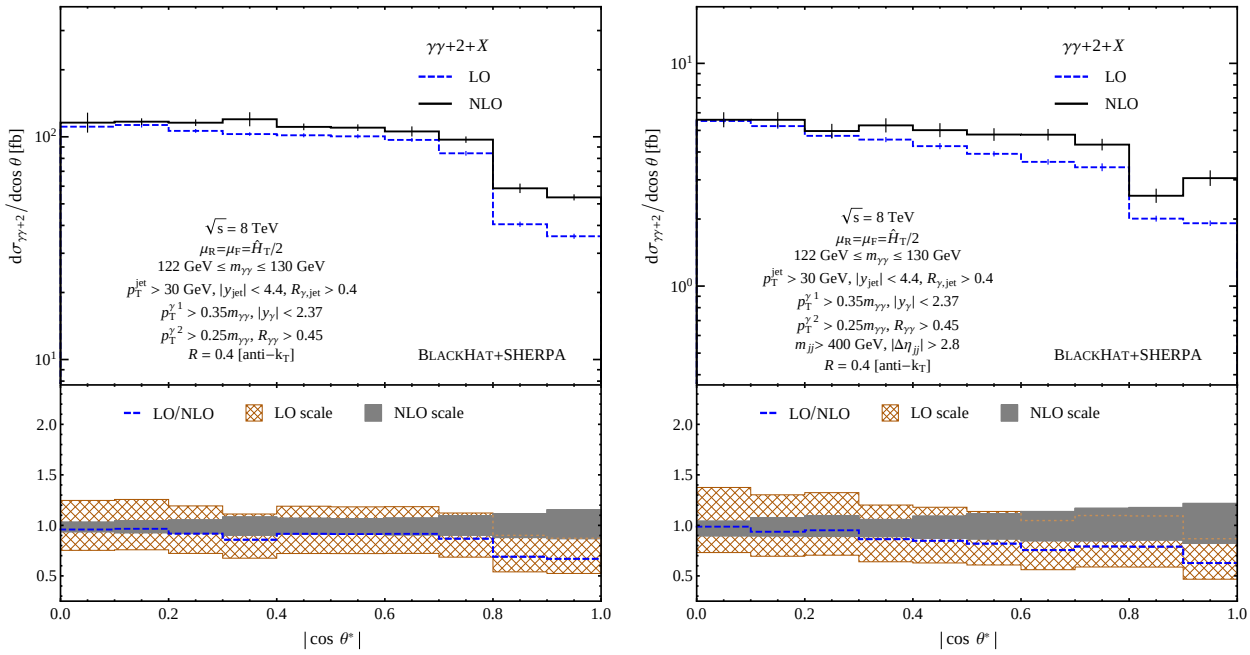

FIG. 16: The distribution of $|\cos\theta^*|$, as defined in eq. (2.19), in $\gamma\gamma$ + 2-jet production. The left plot shows the distribution for the ATLAS cuts of eq. (2.13), and the right plot with the VBF cuts of eq. (2.11) in addition. The panels, curves, and bands are as in fig. 8.

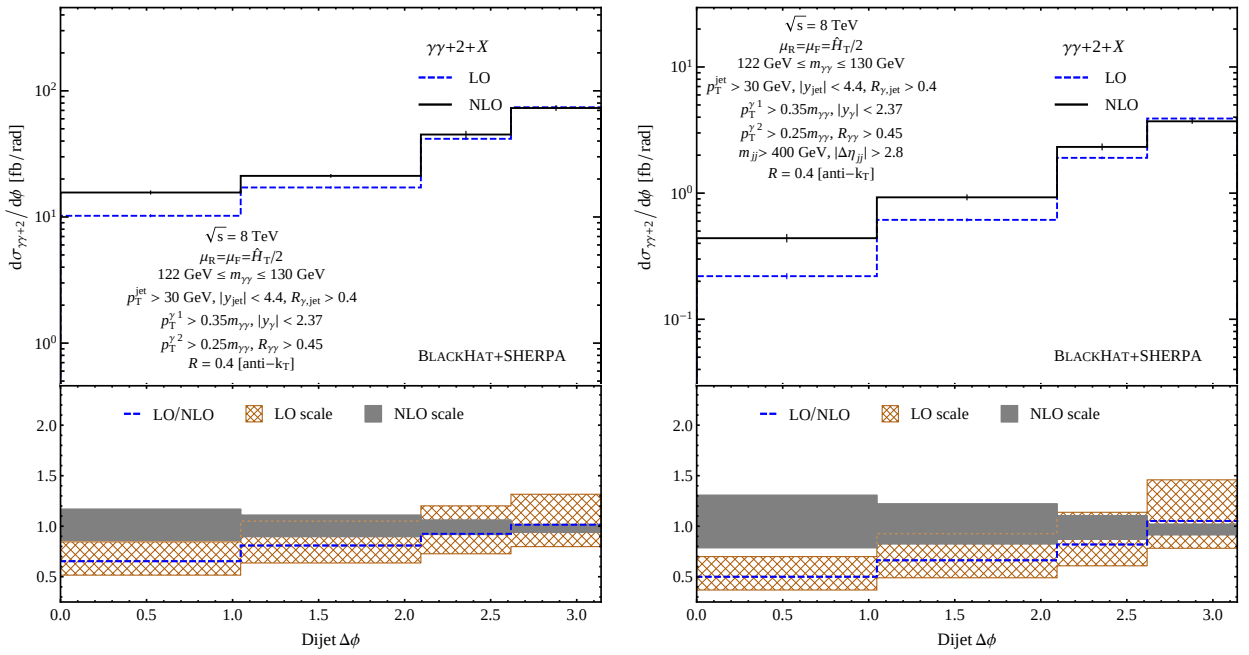

FIG. 17: The distribution of the azimuthal angle between the two leading jets in $\gamma\gamma$ + 2-jet production. The left plot shows the distribution for the ATLAS cuts of eq. (2.13), and the right plot with the VBF cuts of eq. (2.11) in addition. The panels, curves, and bands are as in fig. 8.

In figs. 14–17, we show a series of distributions side-by-side for the ATLAS cuts of eq. (2.13) and for the same cuts with the addition of the VBF cuts of eq. (2.11): in fig. 14, the transverse momentum of the photon pair; in fig. 15, the absolute value of the rapidity of the photon pair; in fig. 16, the absolute value of $\cos\theta^*$, as defined in eq. (2.19); and in fig. 17, the azimuthal angle difference between the leading two jets.

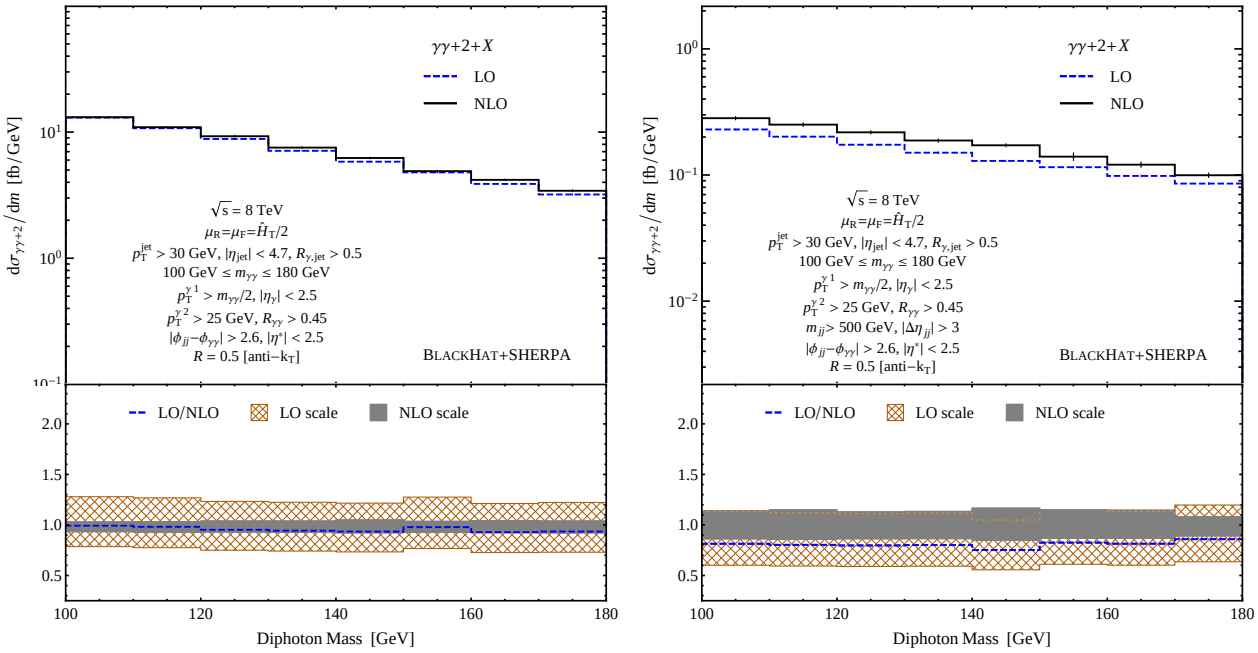

FIG. 18: The photon-pair invariant-mass distribution in $\gamma\gamma+$ 2-jet production. The left plot shows the distribution for the CMS cuts of eq. (2.14), and the right plot with the VBF cuts of eq. (2.16) in addition. The panels, curves, and bands are as in fig. 8.

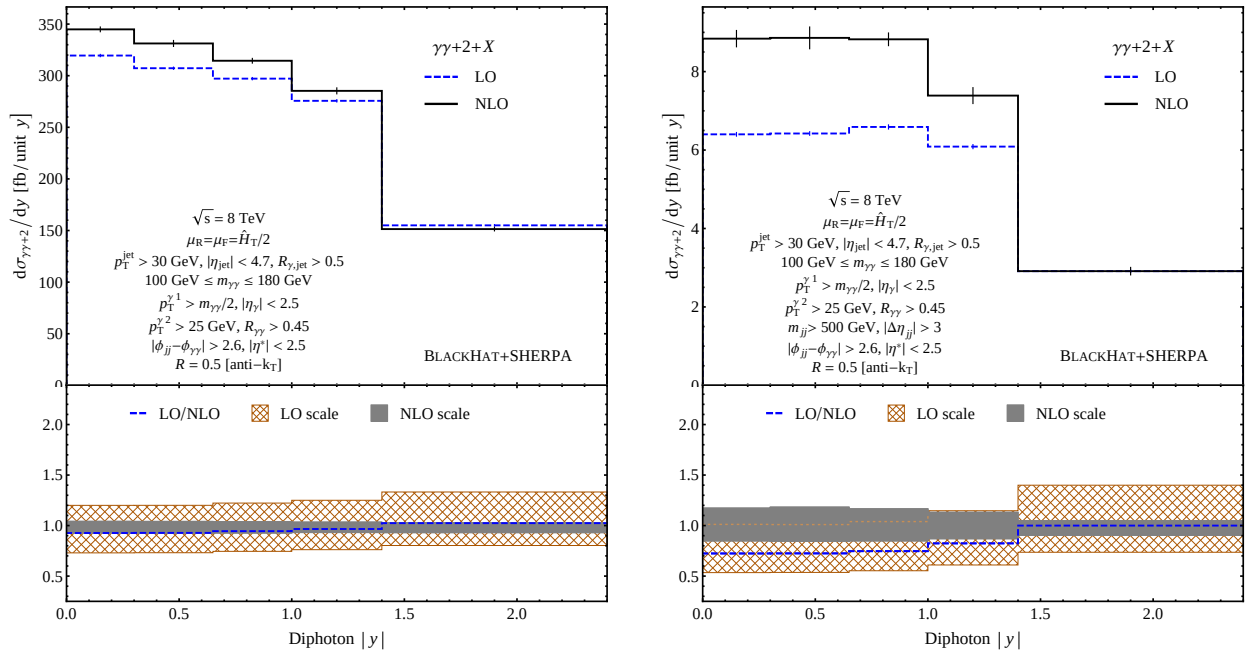

FIG. 19: The distribution of the absolute value of the diphoton rapidity in $\gamma\gamma+$ 2-jet production. The left plot shows the distribution for the CMS cuts of eq. (2.14), and the right plot with the VBF cuts of eq. (2.16) in addition. The panels, curves, and bands are as in fig. 8.

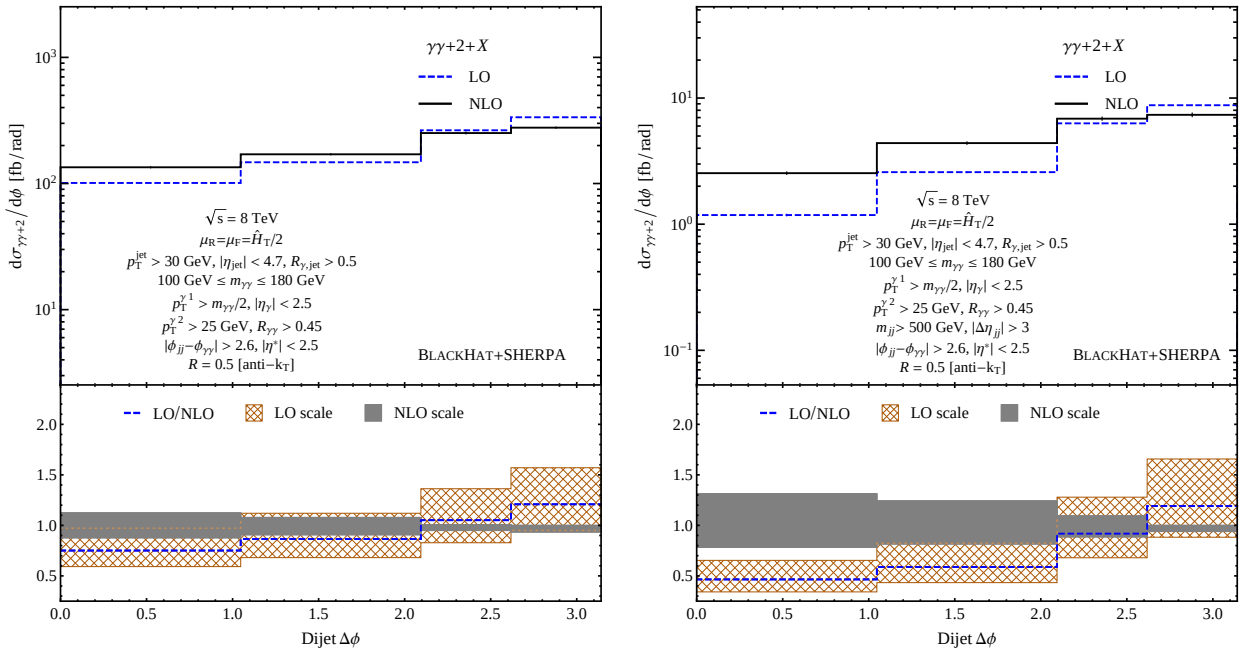

FIG. 20: The distribution of the azimuthal angle between the two leading jets in $\gamma\gamma$ + 2-jet production. The left plot shows the distribution for the CMS cuts of eq. (2.14), and the right plot with the VBF cuts of eq. (2.16) in addition. The panels, curves, and bands are as in fig. 8.

In figs. 18–20, we show three distributions side-by-side for the CMS cuts of eq. (2.14) and for the same cuts with the addition of the VBF cuts of eq. (2.16): in fig. 18, the invariant mass distribution of the photon pair; in fig. 19, the absolute value of the rapidity of the photon pair; and in fig. 20, the azimuthal angle difference between the leading two jets.

The leading-jet transverse-momentum distribution, shown in the left plot in fig. 8, is fairly typical in many respects. The upper panel shows the distribution itself. Because it is steeply falling, several features are easier to see in the ratio to the central NLO prediction, shown in the lower panel. The NLO prediction is somewhat softer than the LO one; that is, it falls somewhat faster, as seen in the upward slope of the dashed blue line in the lower panel. The scale-dependence bands are shown in hatched orange-brown at LO, and gray at NLO. The NLO band is narrower than the LO one throughout, as expected, and is within 10–15% of the central value throughout most of the range. In the lowest $p_{\rm T}$ bin, the NLO correction is significant — the LO prediction is about 30% lower than the NLO one. This is accompanied by a wider scale-dependence band in this bin. The VBF cuts push the peak of the NLO distribution to around 70 GeV, as shown in the right plot of fig. 8, from the cut value of 50 GeV. The lower bins have larger NLO corrections, and correspondingly larger scale dependence.

We show the same distribution with ATLAS cuts in fig. 9. These cuts flatten the distribution somewhat (note that the plots cut off at a lower transverse momentum than in fig. 8). The shape corrections are again more noticeable after VBF cuts, and the scale dependence remains large even at NLO in the lowest bins, where the LO prediction is nearly 50% lower than the NLO one.

The transverse-momentum distributions of the second jet and of the leading photon are shown in fig. 10 and fig. 11, respectively. The VBF cuts do not alter the shape of the photon p_{T} distribution much. The NLO corrections soften the distribution in a manner typical for p_{T} distributions. The softening is particularly pronounced for the second-jet p_{T} distribution after VBF cuts.

The distribution of the dijet invariant mass, shown in the left plot of fig. 12, has a peak around 100 GeV sculpted by the cuts of eq. (2.10). If we impose VBF cuts, the lower part of the distribution is cut out, and we are left only with the high-mass tail shown in the right plot of fig. 12. In the latter case, the LO and NLO distributions are similar in shape. The same is true for the distribution without VBF cuts, in the peak region and above. At low invariant mass, in contrast, the NLO corrections are large and the NLO scale dependence remains substantial.

This can be understood as follows. Given the minimum p_{T}s imposed on the jets, small dijet invariant masses arise primarily from a small angular separation between the jets. In this region, the LO matrix element approaches a collinear factorization limit, where it becomes a lower-point matrix element, with only three massless objects (two photons and one parton) in the final state. Let us consider the real-emission corrections to the LO process in this region, compared to the real-emission corrections at a generic point in the LO process's phase space. The phase space for three massless final-state objects is more constrained than the one for four massless final-state objects; and the additional constraints are more significant than in comparing the phase space for four massless final-state objects with one for five objects. Accordingly, the additional emission of a gluon has a relatively larger phase space to fill, so the additional emission relaxes kinematic constraints in a more substantial way than at a generic point in phase space. This is similar to the larger corrections seen in three-jet production compared to four-jet production, or in W + 2-jet production compared to W + 3-jet production.

The distribution of the photon pair's invariant mass, shown in fig. 13, has a peak around

100 GeV sculpted by the cuts of eq. (2.10). In the peak region and above, the distribution has modest NLO corrections, and its shape is somewhat hardened by VBF cuts. In these regions, the scale dependence narrows significantly at NLO. At low invariant mass, in contrast, the NLO corrections are again large and the NLO scale dependence remains substantial, even more so than for the dijet mass distribution. Here this is true whether VBF cuts are imposed or not. Once again, small invariant masses arise from a small angular separation, in this case of the photons instead of the jets. In this region, while the LO matrix element does not factorize (there is no collinear singularity for a photon pair), the kinematics again resembles that of a lower-point matrix element, with only three massless objects in the final state. Once again the kinematic relaxation in the real-emission corrections is more significant than at a generic point in phase space. The CMS cuts (2.14) restrict attention to sufficiently large values of the di-photon invariant mass, shown in fig. 18, that the NLO corrections remain modest in magnitude, and do not alter the shape of the distribution, both before and after VBF cuts.

If we had no jets, or only one jet, in the final state, in addition to the pair of photons, then restricting the photon-pair transverse momentum to small values would impose a strong constraint on additional radiation; we would expect to see large corrections from a mismatch between virtual and real-emission contributions there. With two jets in the final state, however, such a restriction imposes no constraint on additional radiation, and the corrections should be small. This is what we see if we examine the transverse momentum distribution of the photon pair, shown in fig. 14, both before and after VBF cuts. The shape of this distribution has only small corrections at NLO. It is influenced by the restriction (suggested by ATLAS) to a photon-pair mass window around the mass of the Higgs-like boson. The shape of the photon-pair rapidity distribution, shown subject to ATLAS cuts and folded over to positive values in fig. 15, is similarly unaffected by NLO corrections before VBF cuts; the photon pair tends to be produced centrally. In contrast, after VBF cuts are applied the NLO distribution becomes somewhat more central than the LO prediction. With the CMS cuts, shown in fig. 19, the corrections to the shape are similarly modest before VBF cuts, but even more significant after VBF cuts than for the corresponding ATLAS cuts.

The distribution with respect to the Collins-Soper angle $|\cos\theta^*|$ defined in eq. (2.19) is shown in fig. 16. The shapes of these distributions are also similar at NLO and LO, both before and after VBF cuts.

We show the distribution of the azimuthal angle separation between the two leading jets, using ATLAS cuts, in fig. 17. The jets are somewhat more decorrelated at NLO, as might be expected from the addition of radiation. This effect is much stronger after VBF cuts, so that at smaller angles (< 1 radian), the LO prediction is only half of the NLO one, and the NLO scale dependence is correspondingly larger. The effects are similar when applying CMS cuts, as shown in fig. 20, again with a stronger effect after applying VBF cuts.

IV. CONCLUSIONS

In this paper, we have studied the inclusive production of a photon pair in association with two jets, at NLO in perturbative QCD. This final state is an important background to the study of the Higgs-like boson [1] decaying into a photon pair in the vector-boson fusion production channel. We have employed a Frixione-style isolation criterion for the photon. While this criterion does not correspond precisely to experimental practice, given current practice and various uncertainties in traditional cone isolation, it is likely to be useful as a theoretical prediction. We have examined the cross section and a variety of distributions under three different pairs of cuts. Each pair contains a 'standard' set of cuts, corresponding to generic production of this final state, and an additional set of cuts restricting the phase space to that corresponding to searches for Higgs boson production via vector-boson fusion. We have made the n-tuple files [29] used publicly available, in process directories `YY2j` and `YY2j_VBF`, as explained in section II D. (The location of these directories may be found in `http://blackhat.hepforge.org/trac/wiki/Location`.) One pair of cuts uses fairly generic jet and photon transverse momentum cuts, while the other two pairs use cuts suggested by CMS and ATLAS, which also restrict attention to a window in the photon-pair invariant mass surrounding the Higgs-like boson mass. In the total cross section and in most parts of distributions, we find that the NLO scale dependence is reduced to 10–15%, so that the NLO prediction should be quantitatively reliable. In some bins of some distributions, the NLO corrections alter the LO prediction quite substantially, and in these cases the scale dependence at NLO remains substantially larger. These features suggest that the NLO corrections will play an important role in upcoming experimental analyses of data from the next run of the LHC.

Acknowledgments

We thank Joey Huston for discussions about photon isolation and photon physics. We also thank Nicolas Greiner and Marco Pieri for discussions. FFC and NALP thank the LPNHE for its hospitality, and FFC acknowledges partial support by ECOS Nord, while the research reported here was being completed. This research was supported by the US Department of Energy under contracts de–sc0009937 and DE–AC02–76SF00515. DAK and NALP's research is supported by the European Research Council under Advanced Investigator Grant ERC–AdG–228301. DM's work was supported by the Research Executive Agency (REA) of the European Union under the Grant Agreement number PITN–GA–2010–264564 (LHCPhenoNet). ZB, LJD, SH, HI, DAK and NALP would also like to thank the Simons Center Geometry and Physics for hospitality, where this work was finalized. This research used resources of Academic Technology Services at UCLA.

Appendix A: Tables of Distributions for Basic and VBF Cuts

In this appendix, we provide tables for the kinematical distributions displayed and discussed in section III. All tables show differential cross sections at both LO and NLO, with numerical integration uncertainties given in parentheses, and scale-dependence bands indicated by super- and subscripts. For distributions in dimensionful variables, the variables are given in GeV, and the units for the distributions are femtobarns per GeV. We display results both with the cuts of eq. (2.10), shown in columns marked with 'Basic', and these cuts supplemented by the VBF cuts of eq. (2.11), shown in columns marked with 'VBF'. In Table II, we display the leading-jet transverse-momentum distribution; in Table III, the second-jet transverse-momentum distribution; in Table IV, the leading-photon transverse-momentum distribution; and in Table V, the photon-pair invariant-mass distribution.

The dijet invariant-mass distribution has different ranges for the standard and VBF cuts; we display the results for the two sets of cuts in separate tables: in Table VI, the distribution for the cuts of eq. (2.10), and in Table VII, the distribution with these cuts supplemented by the VBF cuts of eq. (2.11).

p_{T}	LO		NLO	
	Basic	VBF	Basic	VBF
40–60	$32.13(0.09)^{+9.27}_{-6.71}$	$0.611(0.005)^{+0.251}_{-0.163}$	$41.0(0.3)^{+4.9}_{-4.6}$	$0.99(0.02)^{+0.24}_{-0.18}$
60–80	$27.58(0.07)^{+8.14}_{-5.85}$	$0.933(0.004)^{+0.370}_{-0.244}$	$34.3(0.3)^{+3.7}_{-3.7}$	$1.36(0.06)^{+0.25}_{-0.22}$
80–100	$20.09(0.05)^{+6.05}_{-4.32}$	$1.078(0.004)^{+0.416}_{-0.276}$	$24.4(0.4)^{+2.3}_{-2.5}$	$1.29(0.06)^{+0.14}_{-0.16}$
100–120	$14.82(0.05)^{+4.52}_{-3.22}$	$1.059(0.005)^{+0.402}_{-0.269}$	$17.0(0.2)^{+1.3}_{-1.6}$	$1.18(0.02)^{+0.10}_{-0.13}$
120–140	$10.72(0.04)^{+3.31}_{-2.35}$	$0.883(0.004)^{+0.334}_{-0.223}$	$10.8(0.2)^{+0.2}_{-0.7}$	$0.90(0.02)^{+0.02}_{-0.08}$
140–160	$7.44(0.03)^{+2.33}_{-1.65}$	$0.665(0.003)^{+0.251}_{-0.168}$	$7.8(0.1)^{+0.3}_{-0.6}$	$0.66(0.05)^{+0.02}_{-0.06}$
160–180	$5.15(0.02)^{+1.64}_{-1.15}$	$0.471(0.003)^{+0.179}_{-0.120}$	$5.09(0.09)^{+0.10}_{-0.34}$	$0.42(0.01)^{+0.00}_{-0.03}$
180–200	$3.56(0.02)^{+1.14}_{-0.80}$	$0.324(0.002)^{+0.124}_{-0.083}$	$3.51(0.08)^{+0.06}_{-0.24}$	$0.31(0.01)^{+0.00}_{-0.02}$
200–220	$2.51(0.01)^{+0.82}_{-0.57}$	$0.224(0.002)^{+0.086}_{-0.058}$	$2.52(0.04)^{+0.04}_{-0.17}$	$0.188(0.009)^{+0.000}_{-0.012}$
220–240	$1.81(0.01)^{+0.59}_{-0.42}$	$0.156(0.002)^{+0.060}_{-0.040}$	$1.72(0.04)^{+0.02}_{-0.11}$	$0.146(0.006)^{+0.002}_{-0.011}$
240–260	$1.32(0.01)^{+0.44}_{-0.31}$	$0.108(0.001)^{+0.042}_{-0.028}$	$1.29(0.04)^{+0.02}_{-0.09}$	$0.088(0.005)^{+0.000}_{-0.006}$

TABLE II: The leading-jet transverse-momentum distribution, in fb/GeV, in $\gamma\gamma+$ 2-jet production, as shown in fig. 8.

p_{T}	LO		NLO	
	Basic	VBF	Basic	VBF
25–45	$71.8(0.1)^{+21.3}_{-15.3}$	$2.332(0.009)^{+0.922}_{-0.608}$	$83.5(0.6)^{+7.1}_{-8.0}$	$2.86(0.06)^{+0.39}_{-0.39}$
45–65	$28.87(0.06)^{+8.75}_{-6.24}$	$1.775(0.005)^{+0.685}_{-0.455}$	$35.6(0.3)^{+3.5}_{-3.7}$	$2.12(0.03)^{+0.20}_{-0.26}$
65–85	$12.77(0.03)^{+3.95}_{-2.80}$	$1.182(0.004)^{+0.446}_{-0.298}$	$15.1(0.1)^{+1.4}_{-1.5}$	$1.32(0.02)^{+0.11}_{-0.15}$
85–105	$6.58(0.02)^{+2.06}_{-1.46}$	$0.664(0.002)^{+0.250}_{-0.168}$	$7.50(0.07)^{+0.51}_{-0.69}$	$0.70(0.01)^{+0.04}_{-0.07}$
105–125	$3.78(0.02)^{+1.20}_{-0.84}$	$0.346(0.002)^{+0.132}_{-0.088}$	$4.22(0.04)^{+0.28}_{-0.38}$	$0.333(0.009)^{+0.006}_{-0.027}$
125–145	$2.32(0.01)^{+0.74}_{-0.52}$	$0.191(0.001)^{+0.074}_{-0.049}$	$2.44(0.04)^{+0.06}_{-0.19}$	$0.173(0.005)^{+0.003}_{-0.013}$
145–165	$1.50(0.01)^{+0.49}_{-0.34}$	$0.1119(0.0009)^{+0.0436}_{-0.0290}$	$1.58(0.03)^{+0.07}_{-0.13}$	$0.100(0.004)^{+0.001}_{-0.007}$
165–185	$0.996(0.007)^{+0.325}_{-0.227}$	$0.0670(0.0007)^{+0.0263}_{-0.0175}$	$1.02(0.02)^{+0.03}_{-0.08}$	$0.049(0.005)^{+0.001}_{-0.008}$
185–205	$0.700(0.007)^{+0.230}_{-0.161}$	$0.0423(0.0005)^{+0.0167}_{-0.0111}$	$0.75(0.03)^{+0.04}_{-0.06}$	$0.038(0.002)^{+0.000}_{-0.002}$
205–225	$0.497(0.005)^{+0.165}_{-0.115}$	$0.0274(0.0004)^{+0.0109}_{-0.0072}$	$0.46(0.03)^{+0.01}_{-0.03}$	$0.022(0.002)^{+0.000}_{-0.002}$
225–245	$0.356(0.004)^{+0.119}_{-0.083}$	$0.0188(0.0004)^{+0.0075}_{-0.0050}$	$0.32(0.02)^{+0.00}_{-0.01}$	$0.014(0.001)^{+0.000}_{-0.001}$
245–265	$0.256(0.003)^{+0.086}_{-0.060}$	$0.0129(0.0003)^{+0.0052}_{-0.0034}$	$0.24(0.02)^{+0.00}_{-0.01}$	$0.007(0.001)^{+0.001}_{-0.003}$

TABLE III: The second-jet transverse-momentum distribution in fb/GeV in $\gamma\gamma+$ 2-jet production, as shown in fig. 10.

p_{T}	LO		NLO	
	Basic	VBF	Basic	VBF
50–70	$49.85(0.09)^{+14.50}_{-10.46}$	$2.238(0.006)^{+0.862}_{-0.573}$	$60.1(0.3)^{+5.7}_{-6.0}$	$2.69(0.03)^{+0.31}_{-0.35}$
70–90	$29.33(0.07)^{+8.76}_{-6.27}$	$1.436(0.005)^{+0.555}_{-0.368}$	$35.5(0.3)^{+3.4}_{-3.6}$	$1.73(0.04)^{+0.20}_{-0.22}$
90–110	$18.47(0.05)^{+5.63}_{-4.01}$	$0.947(0.004)^{+0.367}_{-0.244}$	$21.6(0.4)^{+1.9}_{-2.1}$	$1.07(0.02)^{+0.11}_{-0.13}$
110–130	$11.65(0.04)^{+3.61}_{-2.56}$	$0.634(0.003)^{+0.246}_{-0.163}$	$13.0(0.2)^{+0.8}_{-1.1}$	$0.73(0.02)^{+0.06}_{-0.08}$
130–150	$7.31(0.04)^{+2.31}_{-1.63}$	$0.444(0.003)^{+0.172}_{-0.114}$	$8.02(0.09)^{+0.50}_{-0.74}$	$0.48(0.01)^{+0.03}_{-0.05}$
150–170	$4.68(0.02)^{+1.50}_{-1.06}$	$0.308(0.003)^{+0.120}_{-0.080}$	$5.0(0.1)^{+0.2}_{-0.4}$	$0.33(0.02)^{+0.02}_{-0.03}$
170–190	$3.02(0.02)^{+0.99}_{-0.69}$	$0.219(0.002)^{+0.085}_{-0.057}$	$3.22(0.05)^{+0.14}_{-0.28}$	$0.216(0.008)^{+0.008}_{-0.018}$
190–210	$2.06(0.02)^{+0.68}_{-0.47}$	$0.154(0.002)^{+0.060}_{-0.040}$	$2.14(0.03)^{+0.08}_{-0.17}$	$0.11(0.03)^{+0.00}_{-0.01}$
210–230	$1.37(0.01)^{+0.46}_{-0.32}$	$0.110(0.001)^{+0.043}_{-0.028}$	$1.43(0.03)^{+0.04}_{-0.11}$	$0.097(0.006)^{+0.000}_{-0.006}$

TABLE IV: The leading-photon transverse-momentum distribution in fb/GeV in $\gamma\gamma$ + 2-jet production, as shown in fig. 11.

$m_{\gamma\gamma}$	LO		NLO	
	Basic	VBF	Basic	VBF
0–20	$0.117(0.004)^{+0.034}_{-0.025}$	$0.0052(0.0003)^{+0.0020}_{-0.0013}$	$0.23(0.01)^{+0.05}_{-0.04}$	$0.008(0.002)^{+0.003}_{-0.002}$
20–40	$4.33(0.03)^{+1.27}_{-0.92}$	$0.220(0.002)^{+0.085}_{-0.056}$	$7.9(0.4)^{+1.7}_{-1.3}$	$0.365(0.007)^{+0.083}_{-0.066}$
40–60	$7.94(0.03)^{+2.35}_{-1.69}$	$0.395(0.003)^{+0.153}_{-0.102}$	$11.6(0.2)^{+1.9}_{-1.5}$	$0.566(0.009)^{+0.111}_{-0.091}$
60–80	$13.57(0.05)^{+3.98}_{-2.86}$	$0.616(0.003)^{+0.240}_{-0.159}$	$17.0(0.1)^{+1.9}_{-1.9}$	$0.80(0.01)^{+0.12}_{-0.11}$
80–100	$22.31(0.07)^{+6.50}_{-4.69}$	$0.944(0.004)^{+0.370}_{-0.245}$	$24.7(0.3)^{+1.7}_{-2.1}$	$1.15(0.03)^{+0.13}_{-0.15}$
100–120	$20.92(0.06)^{+6.17}_{-4.44}$	$0.897(0.004)^{+0.351}_{-0.232}$	$23.0(0.2)^{+1.4}_{-1.9}$	$1.01(0.02)^{+0.09}_{-0.12}$
120–140	$15.76(0.05)^{+4.73}_{-3.38}$	$0.706(0.004)^{+0.276}_{-0.183}$	$17.2(0.2)^{+1.0}_{-1.4}$	$0.82(0.01)^{+0.08}_{-0.10}$
140–160	$11.40(0.04)^{+3.47}_{-2.47}$	$0.548(0.003)^{+0.213}_{-0.141}$	$12.5(0.1)^{+0.8}_{-1.1}$	$0.60(0.01)^{+0.05}_{-0.07}$
160–180	$8.18(0.03)^{+2.52}_{-1.79}$	$0.419(0.003)^{+0.162}_{-0.108}$	$8.96(0.09)^{+0.51}_{-0.76}$	$0.46(0.02)^{+0.03}_{-0.05}$
180–200	$5.96(0.03)^{+1.86}_{-1.32}$	$0.333(0.003)^{+0.128}_{-0.085}$	$6.6(0.2)^{+0.4}_{-0.5}$	$0.354(0.009)^{+0.024}_{-0.038}$
200–220	$4.44(0.02)^{+1.40}_{-0.99}$	$0.261(0.003)^{+0.100}_{-0.067}$	$4.97(0.07)^{+0.33}_{-0.46}$	$0.284(0.006)^{+0.021}_{-0.030}$
220–240	$3.31(0.02)^{+1.05}_{-0.74}$	$0.211(0.002)^{+0.080}_{-0.054}$	$3.63(0.04)^{+0.21}_{-0.31}$	$0.18(0.03)^{+0.00}_{-0.01}$
240–260	$2.56(0.02)^{+0.82}_{-0.58}$	$0.175(0.002)^{+0.066}_{-0.044}$	$2.92(0.04)^{+0.20}_{-0.28}$	$0.184(0.008)^{+0.006}_{-0.018}$
260–280	$1.97(0.01)^{+0.64}_{-0.45}$	$0.145(0.001)^{+0.055}_{-0.037}$	$2.26(0.03)^{+0.13}_{-0.20}$	$0.145(0.005)^{+0.003}_{-0.011}$
280–300	$1.54(0.01)^{+0.50}_{-0.35}$	$0.123(0.001)^{+0.046}_{-0.031}$	$1.78(0.03)^{+0.11}_{-0.17}$	$0.118(0.005)^{+0.002}_{-0.009}$

TABLE V: The photon-pair invariant-mass distribution in fb/GeV in $\gamma\gamma$ + 2-jet production, as shown in fig. 13.

m_{jj}	LO	NLO
0–20	$0.67(0.02)^{+0.18}_{-0.13}$	$0.95(0.08)^{+0.14}_{-0.11}$
20–40	$5.26(0.04)^{+1.46}_{-1.07}$	$8.4(0.1)^{+1.5}_{-1.2}$
40–60	$6.08(0.03)^{+1.71}_{-1.25}$	$8.9(0.1)^{+1.3}_{-1.1}$
60–80	$9.53(0.04)^{+2.63}_{-1.93}$	$12.1(0.2)^{+1.4}_{-1.3}$
80–100	$12.53(0.04)^{+3.47}_{-2.55}$	$15.5(0.3)^{+1.7}_{-1.6}$
100–120	$12.70(0.04)^{+3.58}_{-2.61}$	$14.5(0.3)^{+1.0}_{-1.2}$
120–140	$11.63(0.04)^{+3.35}_{-2.43}$	$12.9(0.1)^{+0.8}_{-1.1}$
140–160	$10.08(0.04)^{+2.95}_{-2.13}$	$11.5(0.1)^{+0.9}_{-1.0}$
160–180	$8.59(0.03)^{+2.56}_{-1.84}$	$9.6(0.1)^{+0.6}_{-0.9}$
180–200	$7.28(0.03)^{+2.21}_{-1.58}$	$8.6(0.3)^{+0.7}_{-0.8}$
200–220	$6.20(0.03)^{+1.91}_{-1.36}$	$6.4(0.3)^{+0.3}_{-0.5}$
220–240	$5.28(0.03)^{+1.65}_{-1.17}$	$5.7(0.1)^{+0.3}_{-0.5}$
240–260	$4.41(0.02)^{+1.39}_{-0.98}$	$5.0(0.1)^{+0.4}_{-0.5}$
260–280	$3.80(0.02)^{+1.21}_{-0.85}$	$4.2(0.1)^{+0.3}_{-0.4}$
280–300	$3.27(0.02)^{+1.06}_{-0.74}$	$3.3(0.1)^{+0.1}_{-0.3}$

TABLE VI: The dijet invariant-mass distribution in fb/GeV for standard cuts in $\gamma\gamma$ + 2-jet production, as shown in the left plot in fig. 12.

m_{jj}	LO	NLO
400–420	$0.603(0.004)^{+0.220}_{-0.149}$	$0.67(0.06)^{+0.05}_{-0.07}$
420–440	$0.545(0.003)^{+0.200}_{-0.135}$	$0.68(0.04)^{+0.08}_{-0.09}$
440–460	$0.490(0.003)^{+0.181}_{-0.122}$	$0.55(0.03)^{+0.04}_{-0.06}$
460–480	$0.453(0.003)^{+0.169}_{-0.114}$	$0.55(0.03)^{+0.07}_{-0.07}$
480–500	$0.405(0.003)^{+0.152}_{-0.102}$	$0.43(0.03)^{+0.02}_{-0.04}$
500–520	$0.363(0.002)^{+0.137}_{-0.092}$	$0.43(0.02)^{+0.04}_{-0.05}$
520–540	$0.331(0.002)^{+0.125}_{-0.084}$	$0.35(0.02)^{+0.01}_{-0.03}$
540–560	$0.303(0.002)^{+0.115}_{-0.077}$	$0.36(0.02)^{+0.03}_{-0.04}$
560–580	$0.275(0.002)^{+0.106}_{-0.070}$	$0.33(0.01)^{+0.04}_{-0.04}$
580–600	$0.247(0.002)^{+0.095}_{-0.063}$	$0.27(0.01)^{+0.01}_{-0.03}$
600–620	$0.228(0.002)^{+0.088}_{-0.059}$	$0.28(0.02)^{+0.03}_{-0.03}$

TABLE VII: The dijet invariant-mass distribution in fb/GeV for VBF cuts in $\gamma\gamma+$ 2-jet production, as shown in the right plot in fig. 12.

Appendix B: Tables of Distributions for ATLAS and VBF Cuts

$p_{\rm T}$	LO		NLO	
	ATLAS	VBF	ATLAS	VBF
30–50	$0.86(0.01)^{+0.24}_{-0.18}$	$0.0106(0.0005)^{+0.0044}_{-0.0029}$	$0.99(0.04)^{+0.08}_{-0.09}$	$0.019(0.002)^{+0.005}_{-0.004}$
50–70	$1.10(0.01)^{+0.32}_{-0.23}$	$0.0275(0.0006)^{+0.0112}_{-0.0073}$	$1.31(0.05)^{+0.13}_{-0.14}$	$0.041(0.002)^{+0.008}_{-0.007}$
70–100	$0.743(0.007)^{+0.221}_{-0.158}$	$0.0350(0.0005)^{+0.0136}_{-0.0090}$	$0.80(0.04)^{+0.04}_{-0.07}$	$0.038(0.002)^{+0.003}_{-0.004}$
100–140	$0.366(0.004)^{+0.111}_{-0.079}$	$0.0288(0.0004)^{+0.0110}_{-0.0073}$	$0.42(0.01)^{+0.02}_{-0.03}$	$0.032(0.001)^{+0.002}_{-0.003}$

TABLE VIII: The leading-jet transverse-momentum distribution in fb/GeV in $\gamma\gamma$ + 2-jet production, as shown in fig. 9.

$p_{\rm T}$	LO		NLO	
	ATLAS	VBF	ATLAS	VBF
0–20	$0.465(0.007)^{+0.133}_{-0.096}$	$0.0140(0.0003)^{+0.0055}_{-0.0036}$	$0.42(0.02)^{+0.00}_{-0.02}$	$0.016(0.002)^{+0.002}_{-0.002}$
20–30	$0.90(0.01)^{+0.26}_{-0.19}$	$0.0324(0.0007)^{+0.0127}_{-0.0084}$	$0.90(0.06)^{+0.05}_{-0.06}$	$0.039(0.003)^{+0.005}_{-0.005}$
30–40	$0.97(0.02)^{+0.28}_{-0.20}$	$0.0363(0.0008)^{+0.0141}_{-0.0093}$	$1.09(0.07)^{+0.08}_{-0.10}$	$0.039(0.004)^{+0.001}_{-0.004}$
40–50	$0.97(0.02)^{+0.29}_{-0.21}$	$0.0392(0.0009)^{+0.0153}_{-0.0101}$	$1.05(0.03)^{+0.07}_{-0.08}$	$0.044(0.005)^{+0.005}_{-0.005}$
50–60	$0.88(0.01)^{+0.26}_{-0.19}$	$0.040(0.001)^{+0.016}_{-0.010}$	$0.9(0.1)^{+0.0}_{-0.1}$	$0.048(0.005)^{+0.003}_{-0.005}$
60–80	$0.83(0.01)^{+0.25}_{-0.18}$	$0.0361(0.0007)^{+0.0141}_{-0.0093}$	$0.93(0.03)^{+0.06}_{-0.08}$	$0.039(0.002)^{+0.003}_{-0.005}$
80–100	$0.573(0.008)^{+0.173}_{-0.123}$	$0.0275(0.0006)^{+0.0107}_{-0.0071}$	$0.70(0.01)^{+0.07}_{-0.07}$	$0.033(0.002)^{+0.004}_{-0.004}$
100–200	$0.133(0.001)^{+0.041}_{-0.029}$	$0.0078(0.0001)^{+0.0030}_{-0.0020}$	$0.176(0.003)^{+0.023}_{-0.022}$	$0.0101(0.0004)^{+0.0016}_{-0.0016}$

TABLE IX: The photon-pair transverse-momentum distribution, in fb/GeV, in $\gamma\gamma$ + 2-jet production, as shown in fig. 14.

In this appendix, we provide tables for distributions displayed and discussed in section III. All tables show differential cross sections at both LO and NLO, with numerical integration uncertainties given in parentheses, and scale-dependence bands indicated by super- and subscripts. We display results both with the cuts of eq. (2.13), shown in columns marked with 'ATLAS', and these cuts supplemented by the VBF cuts of eq. (2.11), shown in columns

$\|y\|$	LO		NLO	
	ATLAS	VBF	ATLAS	VBF
0–0.3	$46.0(0.5)^{+13.5}_{-9.7}$	$1.44(0.02)^{+0.55}_{-0.37}$	$53.8(0.9)^{+4.1}_{-4.9}$	$2.04(0.07)^{+0.39}_{-0.31}$
0.3–0.65	$46.1(0.4)^{+13.5}_{-9.7}$	$1.57(0.02)^{+0.60}_{-0.40}$	$54(2)^{+4}_{-5}$	$2.18(0.08)^{+0.41}_{-0.35}$
0.65–1	$47.9(0.5)^{+14.1}_{-10.1}$	$1.92(0.04)^{+0.73}_{-0.49}$	$56(1)^{+5}_{-5}$	$2.38(0.09)^{+0.31}_{-0.35}$
1–1.4	$47.4(0.5)^{+14.1}_{-10.1}$	$2.14(0.03)^{+0.83}_{-0.55}$	$53(1)^{+4}_{-5}$	$2.6(0.1)^{+0.3}_{-0.3}$
1.4–2.4	$23.6(0.3)^{+7.2}_{-5.2}$	$1.41(0.02)^{+0.56}_{-0.37}$	$25(1)^{+1}_{-2}$	$1.36(0.07)^{+0.03}_{-0.12}$

TABLE X: The distribution of the absolute value of the photon-pair rapidity, in fb/unit rapidity, in $\gamma\gamma$ + 2-jet production, as shown in fig. 15.

$\|\cos\theta^*\|$	LO		NLO	
	ATLAS	VBF	ATLAS	VBF
0–0.1	$111(1)^{+33}_{-24}$	$5.5(0.1)^{+2.2}_{-1.4}$	$116(11)^{+4}_{-7}$	$5.6(0.4)^{+0.2}_{-0.6}$
0.1–0.2	$113(2)^{+34}_{-24}$	$5.2(0.1)^{+2.0}_{-1.4}$	$117(3)^{+5}_{-8}$	$5.6(0.4)^{+0.4}_{-0.6}$
0.2–0.3	$106(1)^{+32}_{-23}$	$4.7(0.1)^{+1.9}_{-1.2}$	$116(3)^{+6}_{-9}$	$5.0(0.3)^{+0.5}_{-0.5}$
0.3–0.4	$103(1)^{+31}_{-22}$	$4.55(0.09)^{+1.78}_{-1.18}$	$120(8)^{+10}_{-12}$	$5.3(0.4)^{+0.3}_{-0.6}$
0.4–0.5	$102(2)^{+30}_{-22}$	$4.2(0.1)^{+1.7}_{-1.1}$	$111(3)^{+8}_{-9}$	$5.0(0.3)^{+0.5}_{-0.6}$
0.5–0.6	$100(1)^{+30}_{-21}$	$3.92(0.08)^{+1.53}_{-1.01}$	$110(3)^{+7}_{-9}$	$4.8(0.3)^{+0.6}_{-0.6}$
0.6–0.7	$97(1)^{+28}_{-20}$	$3.61(0.08)^{+1.40}_{-0.93}$	$106(5)^{+8}_{-10}$	$4.8(0.3)^{+0.7}_{-0.7}$
0.7–0.8	$84(2)^{+25}_{-18}$	$3.4(0.1)^{+1.3}_{-0.9}$	$97(3)^{+9}_{-9}$	$4.3(0.2)^{+0.7}_{-0.7}$
0.8–0.9	$40.5(0.9)^{+12.4}_{-8.8}$	$2.01(0.05)^{+0.77}_{-0.51}$	$59(3)^{+7}_{-7}$	$2.5(0.2)^{+0.5}_{-0.4}$
0.9–1	$35.8(0.7)^{+10.9}_{-7.7}$	$1.91(0.04)^{+0.73}_{-0.49}$	$53(1)^{+8}_{-7}$	$3.1(0.2)^{+0.7}_{-0.5}$

TABLE XI: The distribution of the $|\cos\theta^*|$ variable defined in eq. (2.19), in fb, in $\gamma\gamma$ + 2-jet production, as shown in fig. 16.

marked with 'VBF'. In Table VIII, we display the leading-jet transverse-momentum; in Table IX, the photon-pair transverse-momentum distribution (in fb/GeV); in Table X, the distribution of the absolute value of the photon-pair rapidity (in fb/unit rapidity); in Table XI, the distribution in $|\cos\theta^*|$ as defined in eq. (2.19) (in fb); in Table XII, the distribution of

$\Delta\phi_{jj}$	LO		NLO	
	ATLAS	VBF	ATLAS	VBF
0–$\frac{\pi}{3}$	$10.2(0.2)^{+3.0}_{-2.2}$	$0.22(0.01)^{+0.09}_{-0.06}$	$15.6(0.4)^{+2.6}_{-2.2}$	$0.44(0.03)^{+0.13}_{-0.09}$
$\frac{\pi}{3}$–$\frac{2\pi}{3}$	$17.1(0.2)^{+5.1}_{-3.7}$	$0.61(0.01)^{+0.24}_{-0.16}$	$21.2(0.5)^{+2.3}_{-2.2}$	$0.93(0.04)^{+0.20}_{-0.16}$
$\frac{2\pi}{3}$–$\frac{5\pi}{6}$	$41.7(0.5)^{+12.5}_{-8.9}$	$1.90(0.03)^{+0.74}_{-0.49}$	$45(3)^{+3}_{-4}$	$2.3(0.1)^{+0.2}_{-0.3}$
$\frac{5\pi}{6}$–π	$74.1(0.5)^{+22.1}_{-15.8}$	$3.90(0.04)^{+1.51}_{-1.00}$	$73(3)^{+1}_{-5}$	$3.7(0.1)^{+0.1}_{-0.3}$

TABLE XII: The distribution of the azimuthal angle difference between the two leading jets, in fb/radian, in $\gamma\gamma$ + 2-jet production, as shown in fig. 17.

the dijet azimuthal-angle difference (in fb/radian) between the two leading jets.

Appendix C: Tables of Distributions for CMS and VBF Cuts

$m_{\gamma\gamma}$	LO		NLO	
	CMS	VBF	CMS	VBF
100–110	$13.02(0.05)^{+3.76}_{-2.72}$	$0.230(0.002)^{+0.091}_{-0.060}$	$13.1(0.1)^{+0.4}_{-0.9}$	$0.282(0.008)^{+0.040}_{-0.039}$
110–120	$10.73(0.05)^{+3.13}_{-2.26}$	$0.201(0.002)^{+0.080}_{-0.053}$	$10.9(0.1)^{+0.3}_{-0.8}$	$0.251(0.007)^{+0.037}_{-0.036}$
120–130	$8.82(0.04)^{+2.60}_{-1.87}$	$0.174(0.002)^{+0.069}_{-0.045}$	$9.3(0.1)^{+0.4}_{-0.6}$	$0.218(0.006)^{+0.028}_{-0.030}$
130–140	$7.11(0.03)^{+2.12}_{-1.52}$	$0.150(0.002)^{+0.059}_{-0.039}$	$7.53(0.08)^{+0.29}_{-0.56}$	$0.188(0.005)^{+0.025}_{-0.025}$
140–150	$5.83(0.03)^{+1.76}_{-1.26}$	$0.129(0.001)^{+0.051}_{-0.034}$	$6.23(0.07)^{+0.31}_{-0.48}$	$0.172(0.004)^{+0.028}_{-0.026}$
150–160	$4.79(0.03)^{+1.46}_{-1.04}$	$0.115(0.001)^{+0.045}_{-0.030}$	$4.90(0.07)^{+0.17}_{-0.36}$	$0.140(0.009)^{+0.021}_{-0.019}$
160–170	$3.88(0.02)^{+1.19}_{-0.85}$	$0.098(0.001)^{+0.039}_{-0.026}$	$4.18(0.05)^{+0.17}_{-0.32}$	$0.121(0.006)^{+0.018}_{-0.016}$
170–180	$3.20(0.02)^{+0.99}_{-0.70}$	$0.086(0.001)^{+0.034}_{-0.022}$	$3.43(0.05)^{+0.13}_{-0.27}$	$0.100(0.004)^{+0.008}_{-0.011}$

TABLE XIII: The distribution of the invariant mass of the photon pair in fb/GeV in $\gamma\gamma$ + 2-jet production, as shown in fig. 18.

$\lvert y\rvert$	LO		NLO	
	CMS	VBF	CMS	VBF
0–0.3	$320(1)^{+94}_{-68}$	$6.40(0.05)^{+2.54}_{-1.68}$	$345(2)^{+14}_{-25}$	$8.8(0.2)^{+1.5}_{-1.3}$
0.3–0.65	$307(1)^{+90}_{-65}$	$6.42(0.04)^{+2.53}_{-1.67}$	$331(3)^{+14}_{-25}$	$8.9(0.3)^{+1.6}_{-1.4}$
0.65–1	$297(1)^{+87}_{-63}$	$6.59(0.05)^{+2.58}_{-1.71}$	$315(2)^{+13}_{-23}$	$8.8(0.2)^{+1.5}_{-1.3}$
1–1.4	$276(1)^{+81}_{-58}$	$6.09(0.05)^{+2.39}_{-1.58}$	$285(3)^{+9}_{-20}$	$7.4(0.2)^{+1.0}_{-1.0}$
1.4–2.4	$155.0(0.7)^{+46.7}_{-33.5}$	$2.91(0.03)^{+1.16}_{-0.77}$	$151(2)^{+4}_{-11}$	$2.91(0.09)^{+0.14}_{-0.28}$

TABLE XIV: The distribution of the absolute value of the photon-pair rapidity, in fb/unit rapidity, in $\gamma\gamma$ + 2-jet production, as shown in fig. 19.

$\Delta\phi_{jj}$	LO		NLO	
	CMS	VBF	CMS	VBF
0–$\frac{\pi}{3}$	$101.0(0.5)^{+29.7}_{-21.4}$	$1.18(0.02)^{+0.48}_{-0.31}$	$134(1)^{+17}_{-16}$	$2.54(0.06)^{+0.79}_{-0.55}$
$\frac{\pi}{3}$–$\frac{2\pi}{3}$	$147.4(0.5)^{+43.5}_{-31.3}$	$2.59(0.02)^{+1.04}_{-0.68}$	$170(2)^{+13}_{-16}$	$4.39(0.09)^{+1.06}_{-0.81}$
$\frac{2\pi}{3}$–$\frac{5\pi}{6}$	$264.2(0.9)^{+78.1}_{-56.2}$	$6.30(0.04)^{+2.48}_{-1.64}$	$251(4)^{+2}_{-13}$	$6.9(0.2)^{+0.6}_{-0.8}$
$\frac{5\pi}{6}$–π	$335.1(0.9)^{+100.2}_{-71.8}$	$8.77(0.05)^{+3.43}_{-2.27}$	$277(3)^{+0}_{-18}$	$7.4(0.2)^{+0.0}_{-0.4}$

TABLE XV: The distribution of the azimuthal angle difference between the two leading jets, in fb/radian, in $\gamma\gamma$ + 2-jet production, as shown in fig. 20.

In this appendix, we provide tables for distributions displayed and discussed in section III. All tables show differential cross sections at both LO and NLO, with numerical integration uncertainties given in parentheses, and scale-dependence bands indicated by super- and subscripts. We display results both with the cuts of eq. (2.14), shown in columns marked with 'CMS', and these cuts supplemented by the VBF cuts of eq. (2.16), shown in columns marked with 'VBF'. In Table XIII, we display the distribution of the invariant mass of the photon pair, in fb/GeV; in Table XIV, the distribution of the absolute value of the photon-pair rapidity (in fb/unit rapidity); in Table XV, the distribution of the dijet azimuthal-angle difference (in fb/radian) between the two leading jets.

Appendix D: Virtual Matrix Elements at a Point in Phase Space.

In this appendix, we provide reference values of virtual matrix elements. We provide values for the independent matrix elements in $\gamma\gamma$ + 2-jet production at the same point in phase-space as given in eq. (9.1) of ref. [41] with the scale parameter $\mu = M_Z = 91.188$ GeV for both renormalization and factorization scales, with $\alpha_s(M_Z) = 0.120$ and $\alpha_{EM}(0) = 1/137$ to the required precision. We show these values in table XVI. All other matrix elements are obtained from these by crossing, and by adjusting the electromagnetic charges of the quarks appropriately.

For all matrix elements with non-vanishing tree-level values, we quote the values for the ratio of the virtual corrections to the tree-level squared matrix element, following ref. [13].

$\widehat{d\sigma}_V^{(1)}$	Tree-level	$1/\epsilon^2$	$1/\epsilon$	finite
$1_g 2_g \to 3_\gamma 4_\gamma 5_d 6_{\bar{d}}$	$3.722387496 \cdot 10^{-5}$	-8.666666667	-30.997687242	-29.978172584
$1_d 2_{\bar{d}} \to 3_\gamma 4_\gamma 5_u 6_{\bar{u}}$	$1.726257408 \cdot 10^{-7}$	-5.333333333	-15.845128704	-12.304984940
$1_d 2_{\bar{d}} \to 3_\gamma 4_\gamma 5_d 6_{\bar{d}}$	$2.344204568 \cdot 10^{-5}$	-5.333333333	-15.947959115	7.0934319706
$d\sigma_{\rm OLS}$	—	—	—	finite
$1_g 2_g \to 3_\gamma 4_\gamma 5_g 6_g$	—	—	—	$9.0522165549 \cdot 10^{-4}$

TABLE XVI: The virtual matrix elements at the point in phase space used in ref. [41]. The first column labels the subprocess and the second gives the tree-level matrix element. The third, fourth and fifth columns give, respectively, the $1/\epsilon^2$, $1/\epsilon$ and finite contributions to the normalized virtual matrix element $\widehat{d\sigma}_V^{(1)}$, following the conventions in ref. [13]. For the subprocess $(1_g 2_g \to 3_\gamma 4_\gamma 5_g 6_g)$ the finite part of the one-loop squared amplitudes $d\sigma_{\rm OLS}$ are given directly. Our conventions, as well as the values of the scale parameters and couplings, are given in the main text of this appendix.

We quote the value of the ratio,

$$\widehat{d\sigma}_V^{(1)} \equiv \frac{1}{8\pi\alpha_S\, c_\Gamma(\epsilon)} \frac{d\sigma_V^{(1)}}{d\sigma^{(0)}}\,, \tag{D1}$$

where we have also separated out the dependence on the strong coupling α_s and the overall factor $c_\Gamma(\epsilon)$, defined by

$$c_\Gamma(\epsilon) = \frac{1}{(4\pi)^{2-\epsilon}} \frac{\Gamma(1+\epsilon)\Gamma^2(1-\epsilon)}{\Gamma(1-2\epsilon)}\,. \tag{D2}$$

In the second column of table XVI we give the value of tree-level matrix element squared for the indicated subprocess.

For the $(1_g 2_g \to 3_\gamma 4_\gamma 5_g 6_g)$ subprocess we give the finite part of the one-loop squared matrix elements $d\sigma_{\rm OLS}$ dressed with couplings and factors of $c_\Gamma(\epsilon)$ directly, because the associated tree-level amplitudes vanish, and poles in $1/\epsilon$ are absent.

[1] G. Aad *et al.* [ATLAS Collaboration], Phys. Lett. B **716**, 1 (2012) [arXiv:1207.7214 [hep-ex]]; S. Chatrchyan *et al.* [CMS Collaboration], Phys. Lett. B **716**, 30 (2012) [arXiv:1207.7235 [hep-ex]].

[2] P. Aurenche, A. Douiri, R. Baier, M. Fontannaz and D. Schiff, Z. Phys. C **29**, 459 (1985);
B. Bailey, J. F. Owens and J. Ohnemus, Phys. Rev. D **46**, 2018 (1992);
B. Bailey and J. F. Owens, Phys. Rev. D **47**, 2735 (1993);
C. Balazs, E. L. Berger, S. Mrenna and C. P. Yuan, Phys. Rev. D **57**, 6934 (1998) [hep-ph/9712471];
T. Binoth, J. P. Guillet, E. Pilon and M. Werlen, Eur. Phys. J. C **16**, 311 (2000) [hep-ph/9911340];
T. Binoth, J. P. Guillet, E. Pilon and M. Werlen, Phys. Rev. D **63**, 114016 (2001) [hep-ph/0012191].

[3] J. M. Campbell, R. K. Ellis and C. Williams, JHEP **1107**, 018 (2011) [arXiv:1105.0020 [hep-ph]].

[4] Z. Bern, A. De Freitas and L. J. Dixon, JHEP **0109**, 037 (2001) [hep-ph/0109078].

[5] Z. Bern, L. J. Dixon and C. Schmidt, Phys. Rev. D **66** (2002) 074018 [hep-ph/0206194].

[6] S. Catani, L. Cieri, D. de Florian, G. Ferrera and M. Grazzini, Phys. Rev. Lett. **108**, 072001 (2012) [arXiv:1110.2375 [hep-ph]].

[7] V. Del Duca, F. Maltoni, Z. Nagy and Z. Trócsányi, JHEP **0304**, 059 (2003) [hep-ph/0303012].

[8] T. Gehrmann, N. Greiner and G. Heinrich, JHEP **1306**, 058 (2013) [arXiv:1303.0824 [hep-ph]].

[9] T. Gehrmann, N. Greiner and G. Heinrich, arXiv:1308.3660 [hep-ph];
T. Gehrmann, N. Greiner and G. Heinrich, arXiv:1311.4754 [hep-ph].

[10] S. Badger, A. Guffanti and V. Yundin, arXiv:1312.5927 [hep-ph].

[11] C. F. Berger, Z. Bern, L. J. Dixon, F. Febres Cordero, D. Forde, H. Ita, D. A. Kosower and D. Maître, Phys. Rev. D **78**, 036003 (2008) [arXiv:0803.4180 [hep-ph]].

[12] T. Gleisberg, S. Höche, F. Krauss, A. Schälicke, S. Schumann and J. C. Winter, JHEP **0402**, 056 (2004) [hep-ph/0311263];
T. Gleisberg, S. Höche, F. Krauss, M. Schönherr, S. Schumann, F. Siegert and J. Winter, JHEP **0902**, 007 (2009) [arXiv:0811.4622 [hep-ph]].

[13] C. F. Berger, Z. Bern, L. J. Dixon, F. Febres Cordero, D. Forde, T. Gleisberg, H. Ita, D. A. Kosower and D. Maître, Phys. Rev. D **80**, 074036 (2009) [arXiv:0907.1984 [hep-ph]].

[14] C. F. Berger, Z. Bern, L. J. Dixon, F. Febres Cordero, D. Forde, T. Gleisberg, H. Ita, D. A. Kosower and D. Maître, Phys. Rev. D **82**, 074002 (2010) [arXiv:1004.1659 [hep-ph]].

[15] Z. Bern, G. Diana, L. J. Dixon, F. Febres Cordero, D. Forde, T. Gleisberg, S. Höche, H. Ita,

D. A. Kosower, D. Maître and K. Ozeren, Phys. Rev. D **84**, 034008 (2011) [arXiv:1103.5445 [hep-ph]].

[16] C. F. Berger, Z. Bern, L. J. Dixon, F. Febres Cordero, D. Forde, T. Gleisberg, H. Ita, D. A. Kosower and D. Maître, Phys. Rev. Lett. **106**, 092001 (2011) [arXiv:1009.2338 [hep-ph]].

[17] H. Ita, Z. Bern, L. J. Dixon, F. Febres Cordero, D. A. Kosower and D. Maître, Phys. Rev. D **85**, 031501 (2012) [arXiv:1108.2229 [hep-ph]].

[18] Z. Bern, L. J. Dixon, F. Febres Cordero, S. Höche, H. Ita, D. A. Kosower, D. Maître and K. J. Ozeren, Phys. Rev. D **88**, 014025 (2013) [arXiv:1304.1253 [hep-ph]].

[19] Z. Bern, G. Diana, L. J. Dixon, F. Febres Cordero, S. Höche, D. A. Kosower, H. Ita, D. Maître and K. Ozeren, Phys. Rev. Lett. **109**, 042001 (2012) [arXiv:1112.3940 [hep-ph]].

[20] Z. Bern, G. Diana, L. J. Dixon, F. Febres Cordero, S. Höche, H. Ita, D. A. Kosower, D. Maître and K. J. Ozeren, Phys. Rev. D **84**, 114002 (2011) [arXiv:1106.1423 [hep-ph]].

[21] Z. Bern, G. Diana, L. J. Dixon, F. Febres Cordero, S. Höche, H. Ita, D. A. Kosower, D. Maître and K. J. Ozeren, Phys. Rev. D **87**, 034026 (2013) [arXiv:1206.6064 [hep-ph]].

[22] S. Chatrchyan *et al.* [CMS Collaboration], JHEP **1108**, 155 (2011) [arXiv:1106.4503 [hep-ex]]; Phys. Rev. Lett. **109**, 171803 (2012) [arXiv:1207.1898 [hep-ex]].

[23] G. Aad *et al.* [ATLAS Collaboration], Phys. Rev. D **85**, 032009 (2012) [arXiv:1111.2690 [hep-ex]]; Phys. Rev. D **85**, 092002 (2012) [arXiv:1201.1276 [hep-ex]]; JHEP **1307**, 032 (2013) [arXiv:1304.7098 [hep-ex]].

[24] G. Ossola, C. G. Papadopoulos and R. Pittau, JHEP **0803**, 042 (2008) [arXiv:0711.3596 [hep-ph]];

J.-C. Winter and W. T. Giele, arXiv:0902.0094 [hep-ph];

P. Mastrolia, G. Ossola, T. Reiter and F. Tramontano, JHEP **1008**, 080 (2010) [arXiv:1006.0710 [hep-ph]];

G. Bevilacqua, M. Czakon, M. V. Garzelli, A. van Hameren, A. Kardos, C. G. Papadopoulos, R. Pittau and M. Worek, Comput. Phys. Commun. **184**, 986 (2013) [arXiv:1110.1499 [hep-ph]];

S. Badger, B. Biedermann, P. Uwer and V. Yundin, Phys. Lett. B **718**, 965 (2013) [arXiv:1209.0098 [hep-ph]]; Comput. Phys. Commun. **184**, 1981 (2013) [arXiv:1209.0100 [hep-ph]];

arXiv:1309.6585 [hep-ph].

[25] G. Cullen, N. Greiner, G. Heinrich, G. Luisoni, P. Mastrolia, G. Ossola, T. Reiter and F. Tramontano, Eur. Phys. J. C **72**, 1889 (2012) [arXiv:1111.2034 [hep-ph]].

[26] R. Brun and F. Rademakers, Nucl. Instrum. Meth. A **389**, 81 (1997).

[27] T. Gleisberg and S. Höche, JHEP **0812**, 039 (2008) [arXiv:0808.3674 [hep-ph]].

[28] S. Catani and M. H. Seymour, Nucl. Phys. B **485**, 291 (1997) [Erratum-ibid. B **510**, 503 (1998)] [hep-ph/9605323].

[29] Z. Bern, L. J. Dixon, F. Febres Cordero, S. Höche, H. Ita, D. A. Kosower and D. Maître, arXiv:1310.7439 [hep-ph].

[30] G. Aad *et al.* [ATLAS Collaboration], Nucl. Phys. B **875**, 483 (2013) [arXiv:1307.6795 [hep-ex]].

[31] S. Chatrchyan *et al.* [CMS Collaboration], Phys. Rev. D **84**, 052011 (2011) [arXiv:1108.2044 [hep-ex]].

[32] S. Frixione, Phys. Lett. B **429**, 369 (1998) [hep-ph/9801442].

[33] M. Cacciari, G. P. Salam and G. Soyez, Eur. Phys. J. C **72**, 1896 (2012) [arXiv:1111.6097 [hep-ph]].

[34] S. Frixione, Z. Kunszt and A. Signer, Nucl. Phys. B **467**, 399 (1996) [hep-ph/9512328].

[35] D. A. Kosower, Phys. Rev. D **57**, 5410 (1998) [hep-ph/9710213];
A. Daleo, T. Gehrmann and D. Maître, JHEP **0704**, 016 (2007) [hep-ph/0612257].

[36] R. Frederix, S. Frixione, F. Maltoni and T. Stelzer, JHEP **0910**, 003 (2009) [arXiv:0908.4272 [hep-ph]].

[37] Z. Bern, L. J. Dixon and D. A. Kosower, Ann. Rev. Nucl. Part. Sci. **46** (1996) 109 [hep-ph/9602280]; Annals Phys. **322** (2007) 1587 [arXiv:0704.2798 [hep-ph]];
R. Britto, J. Phys. A **44** (2011) 454006 [arXiv:1012.4493 [hep-th]];
H. Ita, J. Phys. A **44** (2011) 454005 [arXiv:1109.6527 [hep-th]];
R. K. Ellis, Z. Kunszt, K. Melnikov and G. Zanderighi, Phys. Rept. **518** (2012) 141 [arXiv:1105.4319 [hep-ph]].

[38] Z. Bern, L. J. Dixon, D. C. Dunbar and D. A. Kosower, Nucl. Phys. B **425**, 217 (1994) [hep-ph/9403226]; Nucl. Phys. B **435**, 59 (1995) [hep-ph/9409265].

[39] Z. Bern, L. J. Dixon and D. A. Kosower, Nucl. Phys. B **513**, 3 (1998) [hep-ph/9708239].

[40] J. M. Campbell and R. K. Ellis, Phys. Rev. D **65**, 113007 (2002) [hep-ph/0202176].

[41] C. F. Berger, Z. Bern, L. J. Dixon, D. Forde and D. A. Kosower, Phys. Rev. D **74**, 036009

(2006) [hep-ph/0604195].

[42] W. T. Giele and G. Zanderighi, JHEP **0806** (2008) 038 [arXiv:0805.2152 [hep-ph]].

[43] R. K. Ellis, K. Melnikov and G. Zanderighi, JHEP **0904**, 077 (2009) [arXiv:0901.4101 [hep-ph]]; Phys. Rev. D **80**, 094002 (2009) [arXiv:0906.1445 [hep-ph]].

[44] C. F. Berger, Z. Bern, L. J. Dixon, F. Febres Cordero, D. Forde, T. Gleisberg, H. Ita, D. A. Kosower and D. Maître, Phys. Rev. Lett. **102**, 222001 (2009) [arXiv:0902.2760 [hep-ph]].

[45] G. Bevilacqua, M. Czakon, C. G. Papadopoulos, R. Pittau and M. Worek, JHEP **0909**, 109 (2009) [arXiv:0907.4723 [hep-ph]];
G. Bevilacqua, M. Czakon, C. G. Papadopoulos and M. Worek, Phys. Rev. Lett. **104**, 162002 (2010) [arXiv:1002.4009 [hep-ph]]; Phys. Rev. D **84**, 114017 (2011) [arXiv:1108.2851 [hep-ph]].

[46] T. Melia, K. Melnikov, R. Röntsch and G. Zanderighi, JHEP **1012**, 053 (2010) [arXiv:1007.5313 [hep-ph]]; Phys. Rev. D **83**, 114043 (2011) [arXiv:1104.2327 [hep-ph]];
N. Greiner, G. Heinrich, P. Mastrolia, G. Ossola, T. Reiter and F. Tramontano, Phys. Lett. B **713**, 277 (2012) [arXiv:1202.6004 [hep-ph]].

[47] A. Bredenstein, A. Denner, S. Dittmaier and S. Pozzorini, JHEP **0808**, 108 (2008) [arXiv:0807.1248 [hep-ph]]; Phys. Rev. Lett. **103**, 012002 (2009) [arXiv:0905.0110 [hep-ph]];
T. Binoth, N. Greiner, A. Guffanti, J. P. Guillet, T. Reiter and J. Reuter, Phys. Lett. B **685**, 293 (2010) [arXiv:0910.4379 [hep-ph]];
N. Greiner, A. Guffanti, T. Reiter and J. Reuter, Phys. Rev. Lett. **107**, 102002 (2011) [arXiv:1105.3624 [hep-ph]].

[48] A. Bredenstein, A. Denner, S. Dittmaier and S. Pozzorini, JHEP **1003**, 021 (2010) [arXiv:1001.4006 [hep-ph]].

[49] R. Britto, F. Cachazo and B. Feng, Nucl. Phys. B **725**, 275 (2005) [hep-th/0412103].

[50] R. Britto, F. Cachazo, B. Feng and E. Witten, Phys. Rev. Lett. **94**, 181602 (2005) [hep-th/0501052].

[51] Z. Bern and A. G. Morgan, Nucl. Phys. B **467**, 479 (1996) [hep-ph/9511336];
Z. Bern, L. J. Dixon, D. C. Dunbar and D. A. Kosower, Phys. Lett. B **394** (1997) 105 [hep-th/9611127];
C. Anastasiou, R. Britto, B. Feng, Z. Kunszt and P. Mastrolia, Phys. Lett. B **645** (2007) 213 [hep-ph/0609191];
R. Britto and B. Feng, JHEP **0802**, 095 (2008) [arXiv:0711.4284 [hep-ph]];

W. T. Giele, Z. Kunszt and K. Melnikov, JHEP **0804**, 049 (2008) [arXiv:0801.2237 [hep-ph]];
R. Britto, B. Feng and P. Mastrolia, Phys. Rev. D **78**, 025031 (2008) [arXiv:0803.1989 [hep-ph]];
R. K. Ellis, W. T. Giele, Z. Kunszt and K. Melnikov, Nucl. Phys. B **822** (2009) 270 [arXiv:0806.3467 [hep-ph]].

[52] D. Forde, Phys. Rev. D **75**, 125019 (2007) [arXiv:0704.1835 [hep-ph]].

[53] G. Ossola, C. G. Papadopoulos and R. Pittau, Nucl. Phys. B **763**, 147 (2007) [hep-ph/0609007].

[54] S. D. Badger, JHEP **0901**, 049 (2009) [arXiv:0806.4600 [hep-ph]].

[55] Z. Bern, L. J. Dixon and D. A. Kosower, Nucl. Phys. B **437**, 259 (1995) [hep-ph/9409393].

[56] H. Ita and K. Ozeren, JHEP **1202**, 118 (2012) [arXiv:1111.4193 [hep-ph]].

[57] G. P. Lepage, J. Comput. Phys. **27**, 192 (1978).

[58] A. van Hameren and C. G. Papadopoulos, Eur. Phys. J. C **25**, 563 (2002) [hep-ph/0204055].

[59] C. Duhr, S. Höche and F. Maltoni, JHEP **0608**, 062 (2006) [hep-ph/0607057].

[60] F. A. Berends and W. T. Giele, Nucl. Phys. B **306**, 759 (1988).

[61] A. van Hameren, C. G. Papadopoulos and R. Pittau, JHEP **0909**, 106 (2009) [arXiv:0903.4665 [hep-ph]].

[62] M. Cacciari, G. P. Salam and G. Soyez, JHEP **0804**, 063 (2008) [arXiv:0802.1189 [hep-ph]].

[63] D. L. Rainwater, R. Szalapski and D. Zeppenfeld, Phys. Rev. D **54**, 6680 (1996) [hep-ph/9605444].

[64] S. Catani, Y. L. Dokshitzer, M. H. Seymour and B. R. Webber, Nucl. Phys. B **406**, 187 (1993);
G. P. Salam and G. Soyez, JHEP **0705**, 086 (2007) [arXiv:0704.0292 [hep-ph]].

[65] J. C. Collins and D. E. Soper, Phys. Rev. D **16**, 2219 (1977).

[66] G. Aad *et al.* [ATLAS Collaboration], Phys. Lett. B **726**, 120 (2013) [arXiv:1307.1432 [hep-ex]].

[67] CMS Collaboration, CMS-PAS-SMP-13-001.

[68] A. D. Martin, W. J. Stirling, R. S. Thorne and G. Watt, Eur. Phys. J. C **63**, 189 (2009) [arXiv:0901.0002 [hep-ph]].

[69] B. A. Kniehl and L. Lönnblad, DESY 92–032 (1992), in *Proceedings of the Annecy Photon Workshop (1991)*;
A. Czarnecki and W. J. Marciano, Phys. Rev. Lett. **81**, 277 (1998) [hep-ph/9804252].

[70] C. W. Bauer and B. O. Lange, arXiv:0905.4739 [hep-ph];
K. Melnikov and G. Zanderighi, Phys. Rev. D **81**, 074025 (2010) [arXiv:0910.3671 [hep-ph]].